Title

METTL3 is essential for small intestinal epithelial proliferation via regulation of growth factor signaling including KRAS

Authors

Charles H. Danan[1,2,3], Kaitlyn E. Naughton[1], Katharina E. Hayer[4,5,6], Sangeevan Vellappan[7,8,9], Emily A. McMillan[1], Yusen Zhou[1,4], Rina Matsuda[3,10], Shaneice K. Nettleford[1], Kay Katada[1,3], Louis R. Parham[1,3], Xianghui Ma[1], Afrah Chowdhury[1], Benjamin J. Wilkins[6], Premal Shah[8,9], Matthew D. Weitzman[3,5,6], Kathryn E. Hamilton[1,3,11*]

Affiliations

[1]Division of Gastroenterology, Hepatology, and Nutrition; Department of Pediatrics; Children's Hospital of Philadelphia; Perelman School of Medicine, University of Pennsylvania, Philadelphia, PA, 19104, USA;
[2]Medical Scientist Training Program, Perelman School of Medicine, University of Pennsylvania, Philadelphia, PA, 19104, USA;
[3]Perelman School of Medicine, University of Pennsylvania, Philadelphia, PA, 19104, USA;
[4]Department of Biomedical and Health Informatics, The Children's Hospital of Philadelphia, Philadelphia, PA, 19104, USA
[5]Division of Protective Immunity, Children's Hospital of Philadelphia, Philadelphia, PA, 19104, USA;
[6]Department of Pathology and Laboratory Medicine, Perelman School of Medicine; University of Pennsylvania, Philadelphia, PA, 19104, USA;
[7]Waksman Institute of Microbiology, Rutgers University, Piscataway, NJ, 08854, USA;
[8]Department of Genetics, Rutgers University, Piscataway, NJ, 08854, USA;
[9]Human Genetics Institute of New Jersey, Piscataway, NJ, 08854, USA;
[10]Department of Pathobiology, School of Veterinary Medicine, University of Pennsylvania, Philadelphia, PA, 19104, USA;
[11]Institute for Regenerative Medicine, University of Pennsylvania, Philadelphia, PA, 19104, USA.

*Corresponding Author

Kathryn E. Hamilton, PhD
903 Abramson Research Building
Children's Hospital of Philadelphia
3615 Civic Center Blvd.
Philadelphia, PA 19104, USA
267-426-5266
hamiltonk1@chop.edu
@KHamiltonPhD

Abstract

The METTL3-METTL14 methyltransferase complex adds N6-methyladenosine (m^6A) to mRNA with profound impacts on cell fate. Studies delete METTL3 or METTL14 interchangeably to define the role of m^6A in target tissues despite a lack of data confirming that these deletions are equivalent. Intestinal epithelial METTL14 deletion triggers stem cell death in the colon with no overt phenotype in the small intestine. The effect of METTL3 deletion in the same tissues remains unknown. We report that intestinal epithelial METTL3 deletion caused unexpected severe defects in the small intestine, including crypt and villus atrophy associated with cellular senescence and death in the crypt transit amplifying zone. Ribosome profiling and m^6A-sequencing demonstrated downregulated translation of hundreds of unique methylated transcripts, including genes essential to growth factor signal transduction, such as *Kras*. Our study

suggests that METTL3 is essential for small intestinal homeostasis via enhanced translation of growth factor signaling in crypt transit amplifying cells.

Teaser

METTL3 deletion leads to cell death in proliferating small intestinal epithelium associated with decreased translation of growth factor transducers.

MAIN TEXT

Introduction

The intestinal epithelium is responsible for nutrient digestion and absorption, protection against pathogen invasion, and regulation of interactions between mucosal immune cells and the external environment of the gut lumen (*1*). A variety of mature intestinal epithelial cell types from the secretory and absorptive lineages perform these functions. The constant and rapid renewal of intestinal epithelial cells—most are replaced every 3-5 days—is essential to maintaining gut homeostasis (*2*).

Intestinal epithelial cell renewal begins in the crypts, which are invaginations into the mucosa that house intestinal stem cells and stem progenitors. The first step of epithelial renewal occurs at the crypt base. Here, intestinal stem cells expressing the Wnt target gene, Lgr5, divide and initiate differentiation (*3*). However, the primary site of intestinal proliferation is the upper portion of the crypt, a region termed the "transit amplifying zone" (*3*). In the transit amplifying zone, the progeny of Lgr5+ stem cells, known as transit-amplifying cells, undergo successive cycles of rapid division as they migrate up the crypt wall. During this time, transit amplifying cells also differentiate into either the secretory or absorptive lineages, the latter comprising the majority of differentiated epithelium of the gut (*4*). This series of cell divisions is a period of enhanced vulnerability for dividing cells. Here, they are particularly susceptible to genotoxic insults such as irradiation or chemotherapeutics (*5*–*7*). Furthermore, continual homeostatic proliferation exposes them to stressors common to all rapidly dividing cells including: replication stress, oxidative and endoplasmic reticulum stress, and dependency on growth factors and mitogenic signaling (*8*–*11*). Compared to the extensive investigation of Lgr5+ stem cells, the factors that maintain the survival and proliferation of transit amplifying cells remain poorly defined.

Most investigation into the gene regulatory mechanisms maintaining intestinal stem cell homeostasis have emphasized the roles of locally secreted morphogens (*e.g.*, WNT, EGF, BMP, NOTCH) and their transcriptional targets (*12*–*15*). While transcriptional control of intestinal stem cell dynamics is relatively well-defined, the contributions of post-transcriptional and epitranscriptomic regulation to intestinal epithelial homeostasis are only beginning to be understood. Recent studies point to essential roles for the RNA modification, N6-methyladenosine (m^6A), in the intestinal epithelium and in the crypt in particular (*16*–*20*). N6-methyladenosine is the most common covalent modification of RNA, occurring on approximately 25% of mRNA transcripts (*21*, *22*). It acts by recruiting RNA-binding proteins that affect mRNA fate at nearly every level of post-transcriptional gene regulation, but principally RNA stability and translation (*23*).

A highly conserved m^6A "writer" complex installs m^6A co-transcriptionally in the nucleus of eukaryotic cells. At the core of this complex are the writer proteins Methyltransferase-like 3 and 14 (METTL3 and METTL14). Although METTL3 is the catalytic subunit, both METTL3 and METTL14 are widely considered to be essential for the methylating activity of the complex (*24*, *25*). Therefore, deletion of METTL3 and METTL14 are used interchangeably to eliminate and define the role of m^6A in the RNA exome of a cell or tissue type.

Recently, two studies defined the global role of m^6A in intestinal epithelial homeostasis with intestinal epithelial specific deletion of METTL14. These studies found essential functions for METTL14 in the survival of intestinal stem cells and maintenance of epithelial integrity. Intriguingly, these dramatic phenotypes were restricted to the colonic epithelium, and the small intestinal epithelium was spared despite deletion of METTL14 in that tissue as well (*26*, *27*). METTL3 has not been investigated in homeostasis of the intestinal epithelium beyond one study that examined METTL3 deletion in the infection of mouse pups. Mouse pups were grossly normal but sacrificed at postnatal day 12, so the effect of METTL3 deletion beyond this timepoint has not been described (*28*). Studies very rarely compare METTL14 and METTL3 deletion in the same tissue. However, based on the previously described interdependency of METTL3 and METTL14 for m^6A writing (*24*, *25*), we hypothesized that METTL3 deletion would phenocopy METTL14 deletion in the intestinal epithelium.

To determine if METTL3 knockout phenocopied METTL14 knockout in the intestinal epithelium, we deleted METTL3 in murine intestinal epithelium using multiple orthogonal methods in mice and mouse-derived enteroids and colonoids. Based on previously published studies of METTL14 deletion in the gut, we expected to find colonic epithelial defects with small intestinal sparing. Surprisingly, deletion of METTL3 severely disrupted small intestinal epithelial homeostasis with relative sparing of the distal colon. Intestinal epithelial METTL3 knockout led to rapid weight loss and mortality in mice associated with crypt and villus atrophy in the distal small intestine. This gross effect of METTL3 deletion was unchanged when examining embryonic deletion, inducible deletion in adult mice, deletion in microbially-depleted mice, and deletion in mouse-derived enteroids *in vitro*. Mechanistically, loss of METTL3 led to increased cell death in the rapidly proliferating cells of the crypt transit amplifying zone associated with double stranded DNA breaks and cellular senescence. m^6A-RNA-sequencing and ribosome profiling after METTL3 deletion revealed downregulation of methylated transcripts critical to growth factor signaling. This included master growth regulator and proto-oncogene, KRAS. Our data support the conclusion that METTL3 is essential for small intestinal homeostasis at the level of transit amplifying cells. Furthermore, these findings are among the first supporting divergent, METTL14-independent roles for METTL3 in a somatic tissue.

Results

Intestinal epithelial METTL3 deletion leads to growth failure and severe small intestinal defects

Published studies suggested that intestinal epithelial METTL3 is dispensable in development through postnatal day 12, but the consequence beyond that time is not known (*28*). To evaluate the requirement of intestinal epithelial METTL3 for development into adulthood, we generated *Villin-*

Cre;Mettl3-flox/flox mice (*Mettl3*$^{VilCre\Delta/\Delta}$). In these mice, Cre activation deletes METTL3 in the small intestinal and colonic epithelium beginning at approximately embryonic day 12.5 (*29*). *Mettl3*$^{VilCre\Delta/\Delta}$ mice were born with Mendelian distribution (X^2 n=79 p>0.85) and appeared grossly normal at 14 days of age with normal weight compared to littermate controls. From 21 to 28 days of age, *Mettl3*$^{VilCre\Delta/\Delta}$ mice lost an average of 19.8% body weight (95% confidence interval, CI ±3.6) while controls gained 43.8% bodyweight (CI ±13.5) (Fig. 1A). By 29 days of age, *Mettl3*$^{VilCre\Delta/\Delta}$ mice exhibited poor body condition, including emaciation, hunched posture, and non-responsiveness to stimuli (Fig. 1, B and C). Body condition and weight loss in *Mettl3*$^{VilCre\Delta/\Delta}$ mice required 70% of mice to be euthanized between the age of 16-29 days (Fig. 1, A, C, and D). There was no distinction between male and female *Mettl3*$^{VilCre\Delta/\Delta}$ mice with respect to weight, appearance, or survival. Due to the phenotype severity and uniform downward trajectory in mouse weight and appearance in the 4th postnatal week, we elected to euthanize and examine all remaining *Mettl3*$^{VilCre\Delta/\Delta}$ mice and *Mettl3*$^{flox/flox}$ controls at postnatal day 29. From these data, we concluded that mice require intestinal epithelial METTL3 for postnatal growth and survival.

We next examined the intestinal pathology of *Mettl3*$^{VilCre\Delta/\Delta}$ mice to determine the cause of their severe growth failure and mortality. *Mettl3*$^{VilCre\Delta/\Delta}$ mice that were euthanized at postnatal day 29 had shortened small and large intestines. In 2/8 mice we also noted blackened, bloody stool in both small and large intestinal segments (fig. S1A). Western blot of epithelial crypt-enriched protein lysates and *in situ* staining for METTL3 demonstrated depletion of METTL3 in the small intestinal and colonic epithelium, and dot blot confirmed depletion of m^{6}A (fig. S1, B to D). To assess epithelial damage, we applied a composite histopathological score for small intestinal and colonic tissue that included grading of immune cell infiltration, depth of tissue damage, degree of regeneration, extent of crypt and villus degradation, and percent of total tissue involvement. Based on previous studies describing no overt pathology in METTL14-depleted small intestinal epithelium (*26*, *27*), we expected to find minimal small intestinal defects in *Mettl3*$^{VilCre\Delta/\Delta}$ mice. Surprisingly, histopathological scores were substantially elevated in *Mettl3*$^{VilCre\Delta/\Delta}$ small intestine compared to controls, and these effects were more dramatic in the small intestine than in the colon. *Mettl3*$^{VilCre\Delta/\Delta}$ mice displayed severe architectural distortion throughout the small intestine, but damage was most severe in the distal half of the tissue. This included villi shortening and tufting and widespread crypt atrophy alongside occasional hypertrophic regenerative crypts and immune cell invasion (Fig. 1, E to G). We observed a similar pattern of tissue damage in the proximal half of the colon, while the distal colon showed mild crypt shortening and distortion, but general preservation of epithelial architecture (Fig. 1, H and I, and fig. S1E). In summary, pan-intestinal epithelial METTL3 deletion led to unexpected severe defects from the small intestine to the proximal colon with only mild changes in the distal colon.

To determine if the observed epithelial architectural distortion was the result of increased epithelial cell death or diminished proliferation, we evaluated proliferation and apoptosis using Ki67 and TUNEL staining. In terms of proliferation, crypts in the distal small intestine of *Mettl3*$^{VilCre\Delta/\Delta}$ mice distributed towards two extremes in adjacent sections of intestine. They were either hyperplastic and hyperproliferative (containing >45 Ki67+ cells), or hypoplastic and hypo-proliferative (containing <10 Ki67+ cells). This stratification of Ki67 expression suggested severely perturbed proliferative signaling (Fig. 1, J and K). We also found a >10-fold increase in the mean number of TUNEL positive cells in *Mettl3*$^{VilCre\Delta/\Delta}$ mice, with staining enriched in the crypt (Fig. 1L). These data suggest that both disrupted proliferation and cell survival contributed to the observed epithelial defects in *Mettl3*$^{VilCre\Delta/\Delta}$ mice.

We next probed for possible etiologies of small intestinal epithelial distortion by examining the numbers of differentiated epithelial cells in *Mettl3*$^{VilCre\Delta/\Delta}$ mice. Loss of secretory cells can contribute to inflammatory changes in the mucosa due to their important roles in producing mucous, antimicrobial compounds, and stem cell niche factors (*30*, *31*). However, even in areas of severe epithelial distortion, we observed maintenance of MUC2+ secretory goblet cells (Fig. 1M). We found modest reductions in LYZ+ Paneth cells (~2 LYZ+ cells lost per crypt) and a trend toward decreased CHGA+ enteroendocrine cells, which are already rare in the distal small intestine (Fig. 1, N and O). Mucin production, indicated by Alcian blue staining, was also maintained in the small intestine, although we did observe decreased mucin in the proximal colon (fig. S1F). In contrast to modest changes in secretory lineages, we observed a mean 49% decrease in alkaline phosphatase-stained area in the distal half of the small intestine of *Mettl3*$^{VilCre\Delta/\Delta}$ mice compared to controls. This effect was strongest in areas of severe villus shortening, where we observed almost no alkaline phosphatase staining (Fig. 1P). These data suggest general maintenance of secretory cells but a dramatic reduction in mature absorptive enterocytes in *Mettl3*$^{VilCre\Delta/\Delta}$ mice. We propose that the resulting loss of absorptive capacity may underlie the wasting seen in these mice.

Together, these data demonstrate that METTL3 expression is essential during the postnatal period for small intestinal epithelial homeostasis. While *Mettl3*$^{VilCre\Delta/\Delta}$ mice appear grossly normal in the first two weeks, as previously reported (*28*), they uniformly failed to gain weight beyond week three. By the end of the fourth week of life, crypt loss and epithelial destruction was evident in *Mettl3*$^{VilCre\Delta/\Delta}$ jejunum and ileum, while the distal colon exhibited only minor differences compared to *Mettl3*$^{flox/flox}$ controls. The extreme architectural abnormalities in the small intestine with much milder distal colonic damage in *Mettl3*$^{VilCre\Delta/\Delta}$ mice was in stark contrast to *Villin-Cre;Mettl14fl/fl* mice described in recent studies (*26*, *27*). *Villin-Cre;Mettl14fl/fl* mice display significant epithelial abnormalities in the colon only, despite presumed loss of METTL14 in the small intestine since *Villin-Cre* targets both small intestine and colon.

Inducible METTL3 deletion in adult mice leads to lethal weight loss and severe small intestinal distortion

Embryonic deletion of METTL3 led to severe small intestinal defects not seen with METTL14 KO in the small intestine. However, these discrepancies could be due to development-specific roles for METTL3. We also wanted to directly assess the role of METTL3 in the homeostasis of adult intestinal epithelium. For these reasons, we generated tamoxifen-inducible *Villin-CreERT2;Mettl3-fl/fl* mice (*Mettl3*$^{VilCreER\Delta/\Delta}$) and injected them with tamoxifen in adulthood between 8-9 weeks of age (Fig. 2A). We confirmed depletion of METTL3 in inducible *Mettl3*$^{VilCreER\Delta/\Delta}$ mice two days post final tamoxifen injection (fig. S2, A and B). Mice began to lose weight and lost on average 5.1% (CI ±1.2) of starting body weight every two days by one week post final injection (Fig. 2B). Within a week post tamoxifen, multiple mice lost critical amounts of weight (>20% starting body weight), with near complete mortality by 2 weeks post tamoxifen injection (Fig. 2C). Due to the limited survival and uniform decrease in weight by nine days post final injection, we elected to euthanize and analyze all mice at this timepoint. Similar to developmental deletion in *Mettl3*$^{VilCre\Delta/\Delta}$ mice, inducible METTL3 deletion during adulthood led to uniformly severe wasting and mortality.

Intestinal epithelial defects in inducible *Mettl3*$^{VilCreER\Delta/\Delta}$ mice mirrored those seen in *Mettl3*$^{VilCre\Delta/\Delta}$. In the small intestine, we observed simultaneous crypt hypertrophy and loss in addition to villus shortening (Fig. 2, D and E). Histopathological scores for small intestine demonstrated extensive tissue damage in the small intestine, especially the jejunum and ileum. This included increased inflammatory cell invasion, regenerative proliferation, and crypt and villus damage (Fig. 2F). The proximal colon demonstrated similarly severe defects, while the distal colon once again exhibited minimal histological differences compared to control (Fig 2., G to I). Furthermore, aside from a mean ~50% reduction in enteroendocrine cells, secretory cells and mucin production were preserved in the small intestine (Fig. 2, J to L, fig. S2C). And once again, the extent of alkaline phosphatase staining was diminished more than 50% in inducible *Mettl3*$^{VilCreER\Delta/\Delta}$ compared to controls (Fig. 2M). As in prenatal METTL3 deletion, hypo-proliferative and hyper-proliferative crypts interspersed along the length of the distal small intestine (Fig. 2N). Although we noted that many hyper-proliferative crypts were METTL3 negative, some appeared to be derived from METTL3+ cells that escaped recombination (fig. S2D); therefore, we elected to not quantify hyperproliferative crypts in these mice. Finally, TUNEL+ crypt and villus cell death in the small intestine of inducible *Mettl3*$^{VilCreER\Delta/\Delta}$ mice was elevated approximately 10-fold compared to controls, matching our findings in the *Mettl3*$^{VilCre\Delta/\Delta}$ mice (Fig. 2P). Taken together, these data demonstrate that inducible *Mettl3*$^{VilCre\Delta/\Delta}$ mice recapitulate *Mettl3*$^{VilCre\Delta/\Delta}$ mice phenotypes. This suggests that METTL3 is a general requirement of small intestinal epithelial homeostasis, regardless of deletion at embryonic day 12.5 or in adulthood.

We considered whether the differences observed in published METTL14 KO mice and our inducible *Mettl3*$^{VilCreER\Delta/\Delta}$ mice may be due to the large genomic deletion induced by recombination of the *loxP* sites spanning nine exons of the *Mettl3* locus (fig. S3A) (*32*). Furthermore, *Villin-CreERT2* activity is slightly diminished in the colon (*33*), and we observed some persistent METTL3 expression in the colon of inducible *Mettl3*$^{VilCreER\Delta/\Delta}$ mice, where the phenotype was minimal (fig. S2B). To address these concerns, we generated a second inducible METTL3 KO model in which we paired *Villin-CreERT2* with a floxed *Mettl3* allele with *LoxP* sites spanning only exon 4 (*Mettl3*$^{VilCreER\Delta2/\Delta2}$, fig. S3B). Inducible *Mettl3*$^{VilCreER\Delta2/\Delta2}$ mice demonstrated efficient deletion of METTL3 in all targeted tissues (fig. S3C). They also displayed gross and histological features recapitulating those seen in inducible *Mettl3*$^{VilCreER\Delta/\Delta}$ mice, including rapid weight loss and mortality, hypo- and hyper-plastic crypts, preservation of secretory goblet and Paneth cells, and absent colonic defects (fig. S3, D to G). These data using orthogonal modes of genetic deletion further support the conclusion that METTL3 is essential for small intestinal homeostasis.

In summary, deletion of METTL3 in the adult intestinal epithelium leads to severe weight loss and mortality associated with defects in small intestinal epithelial proliferation and survival and depleted mature absorptive enterocytes. The gross and small intestinal defects associated with inducible METTL3 deletion in adult mice closely mirrored defects we observed with constitutive METTL3 deletion at embryonic day 12.5 and could be recapitulated with an alternative floxed *Mettl3* allele. These data strongly suggest METTL3 is required for small intestinal epithelial homeostasis regardless of the mode or timing of genetic deletion.

Intestinal epithelial defects with METTL3 deletion occur independently of intestinal microbiota

Because microbial translocation and inflammatory activation are common causes of morbidity and mortality in mice with intestinal epithelial defects, we examined the contribution of inflammatory processes to the disease seen in inducible *Mettl3*$^{VilCreER\Delta/\Delta}$ mice. We first examined sera of *Mettl3*$^{VilCreER\Delta/\Delta}$ mice for elevated inflammatory cytokines. We were surprised to find that a panel of serum cytokine markers including TNF-α, IL-6, IL-1α, IL-1β, IL-10, IL-12 and IFN-γ was not elevated in *Mettl3*$^{VilCreER\Delta/\Delta}$ mice compared to controls (Fig. 3A). Additionally, spleen size—often positively correlated with degree of whole-body inflammation—was reduced (Fig. 3B). Furthermore, small intestinal and colon lengths—often reduced in inflammatory conditions—were unchanged (Fig. 3, C and D). Taken together, these data suggested a non-inflammatory etiology to morbidity and mortality in *Mettl3*$^{VilCreER\Delta/\Delta}$ mice.

Despite little evidence of an overt inflammatory phenotype, we wanted to directly test the contribution of the intestinal microbiota to the histopathology seen in *Mettl3*$^{VilCreER\Delta/\Delta}$ mice. We depleted *Mettl3*$^{VilCreER\Delta/\Delta}$ and *Mettl3*$^{flox/flox}$ mice of their microbiota by adding an antibiotic cocktail to their drinking water beginning one week before tamoxifen injection (Fig. 3E). Quantitative PCR of genomic 16s rRNA confirmed ~1000 fold depletion of luminal bacteria (Fig. 3F). We observed no change in weight loss or mortality in microbiota-depleted mice compared to *Mettl3*$^{VilCreER\Delta/\Delta}$ on normal drinking water (Fig. 3, G and H). Additionally, their small intestinal epithelium displayed architectural abnormalities mirroring those of *Mettl3*$^{VilCreER\Delta/\Delta}$ on normal drinking water as well (Fig. 3I).

Taken together, these data suggest a non-septic, non-inflammatory cause of severe small intestinal epithelial histopathology in *Mettl3*$^{VilCreER\Delta/\Delta}$ mice. These data also reduce the likelihood that facility-dependent microbial differences contributed to the observed discrepancies between *Mettl3*$^{VilCreER\Delta/\Delta}$ mice and published studies with METTL14 deletion in the intestinal epithelium (*26*, *27*). Finally, the absent inflammatory phenotype in *Mettl3*$^{VilCreER\Delta/\Delta}$ mice contrasts with published data in mice with METTL14 deletion in the intestinal epithelium. Intestinal epithelial METTL14 KO mice demonstrated extensive neutrophilic invasion of colonic mucosa, elevated cytokine markers in the colonic mucosa and serum, and complete rescue of mortality with antibiotic-mediated microbial depletion (*27*).

METTL3 deletion leads to rapid cell death in the transit amplifying zone

The severe intestinal epithelial changes in inducible *Mettl3*$^{VilCreER\Delta/\Delta}$ mice nine days post tamoxifen injection included a complex set of phenotypes, such as adjacent areas of hypertrophic and atrophic crypts and scattered villus and crypt cell death. Some of these changes may be reactive, secondary changes rather than immediately downstream of METTL3 depletion. To observe the earliest changes that occurred after METTL3 deletion in the intestinal epithelium, we examined inducible *Mettl3*$^{VilCreER\Delta/\Delta}$ two days after the final tamoxifen injection. This was the earliest timepoint at which we identified METTL3 deletion by immunoblot and *in situ* staining in small intestinal and colonic epithelial tissue (Fig. 4A and fig. S2, A and B).

At two days after final tamoxifen injection, the proximal and distal small intestinal epithelium of *Mettl3*$^{VilCreER\Delta/\Delta}$ mice demonstrated a ~30% increase in crypt height (Fig. 4B). The change in crypt height was also reflected in an elevated number of Ki67+ cells in inducible *Mettl3*$^{VilCreER\Delta/\Delta}$ tissue (Fig. 4C), and qPCR indicated increased expression of a broad set of transcripts associated with active cycling stem cells

and stem progenitors (Fig. 4D). These data suggested an expansion in the number of proliferating stem cells and stem progenitors in inducible *Mettl3*$^{VilCreER\Delta/\Delta}$ mice two days after tamoxifen injection.

Concurrent with crypt expansion, we identified profound increases in crypt cell death in inducible *Mettl3*$^{VilCreER\Delta/\Delta}$ mice at this same early timepoint. The mean number of TUNEL+ foci per crypt was elevated >20 fold in *Mettl3*$^{VilCreER\Delta/\Delta}$ intestinal epithelium (Fig. 4E). Strikingly, we noted that almost all TUNEL+ foci in *Mettl3*$^{VilCreER\Delta/\Delta}$ small intestine were in the highly proliferative transit amplifying zone found between the crypt base and the crypt-villus junction. We quantified TUNEL+ staining in the crypt base, transit amplifying zone, and villus epithelium of *Mettl3*$^{VilCreER\Delta/\Delta}$ mice and found that the rate of cell death in the transit amplifying zone was three-fold higher than the crypt base and six-folder higher than the villus epithelium (Fig. 4F). These data indicate that METTL3 deletion triggers widespread cell death predominantly in the transit amplifying zone.

Taken together, our data at an early timepoint post-METTL3 deletion show a profound increase in cell death in the transit amplifying zone concurrent with increases in proliferation. This suggests that crypt cell death, rather than reduced proliferation, is the initiating event in the intestinal disease seen in inducible *Mettl3*$^{VilCreER\Delta/\Delta}$ mice. These data support a model in which METTL3 is essential for survival of rapidly replicating small intestinal transit amplifying cells.

METTL3 deletion triggers growth arrest and death in intestinal enteroids

We next wanted to examine the kinetics and mechanism of *Mettl3*$^{VilCreER\Delta/\Delta}$ crypt cell death in an epithelial autonomous *in vitro* culture system. Intestinal crypts can be dissociated and cultured as 3D organoids from the small intestine (enteroids) and colon (colonoids) to evaluate epithelial phenotypes in the absence of stromal or immune cells (*34*). We therefore generated enteroids and colonoids from tamoxifen naive *Mettl3*$^{VilCreER\Delta/\Delta}$ and *Mettl3*$^{flox/flox}$ mice and treated with 4-hydroxytamoxifen (4-OHT) *in vitro* to induce METTL3 deletion. We first monitored enteroid and colonoid death after 4-OHT treatment. Dead enteroids and colonoids were defined as those having a complete opaque appearance, leaking of dead cell debris outside of the enteroid or colonoid lumen, and no change in size over the subsequent 24 hours. Five days after withdrawal of tamoxifen, we observed death of almost all enteroids and proximal colonoids derived from inducible *Mettl3*$^{VilCreER\Delta/\Delta}$ mice (Fig. 5, B and C). Only colonoids from the distal colon of *Mettl3*$^{VilCreER\Delta/\Delta}$ mice survived 4-OHT treatment. In these distal colonoids, immunoblotting confirmed deletion of METTL3 (Fig. 5D). In summary, *Mettl3*$^{VilCreER\Delta/\Delta}$ enteroids and colonoids exhibited phenotypes closely reflecting their source tissue. *In vivo*, METTL3 deletion led to extensive epithelial changes from the proximal small intestine through the proximal colon. *In vitro,* METTL3 deletion led to death of enteroids and colonoids derived from the proximal small intestine through the proximal colon. Both *in vivo* and *in* vitro, the distal colon was largely spared. Death in ileal *Mettl3*$^{VilCreER\Delta/\Delta}$ enteroids was the most robust, so we performed further phenotypic experiments in ileal enteroids.

To precisely map the chronology of enteroid growth and survival after METTL3 deletion, we measured ileal enteroid size and death at each day after 4-OHT treatment of *Mettl3*$^{VilCreER\Delta/\Delta}$ and *Villin-CreERT2* control enteroids. In the first two days after withdrawal of 4-OHT, *Mettl3*$^{VilCreER\Delta/\Delta}$ and *Villin-CreERT2* enteroids demonstrated similar morphology and size. However, *Mettl3*$^{VilCreER\Delta/\Delta}$ enteroids consistently displayed growth arrest at day 3 (Fig. 5, E and F). At this timepoint, we also observed

elevation in the fraction of dead enteroids, and by five days post 4-OHT treatment, ileal enteroids demonstrated complete death, and no enteroids survived to subsequent passages (Fig. 5, E and G).

Given that METTL3 deletion led to small intestinal epithelial death *in vivo* and *in vitro*, but depletion of the essential methyltransferase co-factor METTL14 has previously been reported to have no effect on small intestinal homeostasis, we hypothesized that METTL3 might support intestinal epithelial survival through a non-catalytic mechanism. We reintroduced a non-catalytic METTL3 (DPPW$^{395\text{-}398}$ to APPA$^{395\text{-}398}$) (*35*) to *Mettl3*$^{VilCreER\Delta/\Delta}$ ileal enteroids using a lentiviral construct (METTL3$^{\Delta cat}$). Western and dot blot confirmed rescue of METTL3 expression and depletion of m^{6}A in these enteroids (fig. S4, A and B). Compared to *Mettl3*$^{VilCreER\Delta/\Delta}$, *Mettl3*$^{VilCreER\Delta/\Delta}$ + METTL3$^{\Delta cat}$ enteroids demonstrated delayed cell death through the 4th day post 4-OHT, but still died by day 5 and did not survive to subsequent passages (fig. S4, C to E). Previous reports indicated that METTL3 may act independently of METTL14 as a non-catalytic cytoplasmic regulator of protein translation (*36*–*38*). However, we observed exclusively nuclear staining of endogenous METTL3 in ileal enteroids, likely precluding this possibility (fig. S4F). These data suggest that small intestinal epithelium requires the nuclear, catalytic activity of METTL3 for homeostatic function.

In summary, data from *in vitro* enteroid and colonoid studies recapitulate tissue region-specific cell death phenotypes observed *in vivo*. These data also support the conclusion that epithelial cell death with METTL3 deletion is cell autonomous and not due to interactions of METTL3-depleted epithelial cells with other cell types or microbiota found *in vivo*. Furthermore, enteroid death could not be rescued by reintroduction of a non-catalytic METTL3, suggesting the defects seen in *Mettl3*$^{VilCreER\Delta/\Delta}$ mice are dependent on the catalytic activity of METTL3. Finally, these data also established *Mettl3*$^{VilCreER\Delta/\Delta}$ enteroids as a reliable model of *in vivo* pathologies for subsequent investigation.

METTL3 deletion leads to downregulation of global mRNA translational efficiency and growth factor pathways

Previous studies indicate that m^{6}A induces global changes in mRNA abundance and translational efficiency (*18*, *39*, *40*). In order to identify METTL3 targets that may mediate the intestinal epithelial cell death observed *in vivo* and *in vitro*, we sequenced total RNA and ribosome-protected RNA fragments to assay global changes in RNA abundance and translation after METTL3 deletion. Since METTL3 modifies thousands of transcripts with pleiotropic effects, we elected to analyze *Mettl3*$^{VilCreER\Delta/\Delta}$ ileal enteroids 72 hours after 4-OHT treatment to detect the changes most proximal to METTL3 deletion but prior to cell death. Comparing the approximately 25,000 transcripts detected in both data sets, METTL3 deletion impacted more transcripts at the level of RNA translation than abundance; we found 6,101 transcripts exclusively altered at the level of ribosome protected fragments, 3,004 with changes only in RNA abundance, and 1,374 with changes in both (Figure 6A and Data S1). We next compared the ratio of ribosome protected fragments to mRNA abundance for each transcript to produce the translational efficiency ("TE") of each transcript in METTL3 deleted and control enteroids (*16*, *41*). Averaging all 2,124 transcripts with significant changes in TE, the predominant effect of METTL3 deletion was a reduction in TE. We found 1,747 transcripts exhibiting reduced TE and 377 with increased TE, leading to a mean decrease in TE of 39% across all differentially translated transcripts in *Mettl3*$^{VilCreER\Delta/\Delta}$ enteroids compared to controls (Figure 6B). This novel finding suggests a broad role for METTL3 in supporting translation in

the small intestinal epithelium and underscores the importance of post-transcriptional regulation in maintaining normal intestinal homeostasis.

We next wanted to distinguish between direct and indirect effects of METTL3 deletion by identifying transcripts with altered TE that were putatively methylated by METTL3. We therefore performed m^6A immunoprecipitation and sequencing (m^6A-seq) in small intestinal epithelial crypts of wildtype mice *in vivo*. m^6A-seq yielded 13,763 m^6A peaks within 7,882 unique transcripts (Data S2). These peaks were distributed across the coding sequence and 3' untranslated region, with the highest accumulation at the stop codon, consistent with previous reports (fig. S5A) (*21*, *22*). We also saw expected patterns of m^6A enrichment in positive control (*Myc*) and negative control (*Gapdh*) transcripts (fig. S5B). We next superimposed these m^6A-seq data on our ribosome profiling data. Of the 1,747 transcripts with decreased TE after METTL3 deletion, 363 contained at least one m^6A peak (Fig. 6C). Therefore, about ~20% of genes with decreased TE after METTL3 deletion were putatively methylated by METTL3. This suggested that those direct targets of METTL3 likely had important regulatory roles that dramatically impacted a much broader set of transcripts.

We wanted to define the functional characteristics of the key transcripts that were downregulated after METTL3 deletion and putatively methylated by METTL3. We therefore conducted pathway enrichment analysis on transcripts with both decreased TE and at least one m^6A peak. Using Gene Ontology Biological Process (GOBP) gene sets, we observed the most significant enrichment in transcripts associated with growth factor signaling cascades (Fig. 6E). Amongst these transcripts, we saw the largest magnitude reduction in mean TE for *Kras*, the essential intestinal proto-oncogene and master regulator of the RAF-MEK-ERK MAPK signaling cascade that promotes intestinal epithelial proliferation and survival (Fig. 6F) (*42*). Taken together, our ribosome profiling and m^6A-seq data after METTL3 deletion in the intestinal epithelium suggest a broad reduction in translation efficiency of multiple transcripts, a subset of which are methylated. Furthermore, METTL3 deletion in the small intestinal epithelium precipitates a reduction in translation of transcripts involved in growth factor signaling within the cell, including master epithelial growth regulator, *Kras*.

METTL3 deletion reduces *Kras* methylation and protein expression and induces cellular senescence

We further explored the putative relationship between METTL3 and KRAS expression by examining m^6A enrichment density across the *Kras* gene body as determined by m^6A-seq. These data suggested enrichment of m^6A within the *Kras* transcript at multiple locations, including the 5' UTR, CDS, and 3' UTR (Fig. 7A). To verify m^6A-seq peaks on the *Kras* transcript and determine their dependence on METTL3 expression, we performed m^6A-RNA-immunoprecipitation-qPCR (m^6A-RIP-qPCR) in crypt-enriched lysates from *Mettl3*$^{flox/flox}$ and *Mettl3*$^{VilCreER\Delta/\Delta}$ mice three days after final tamoxifen injection. Using qPCR probes targeting both the *Kras* 5' and 3' UTR we found significant enrichment of both transcript regions in m^6A-RIP fractions. However, only m^6A enrichment in the 3' UTR appeared dependent on METTL3 expression, suggesting that only the 3' UTR harbored a genuine m^6A peak. The 5' UTR peak may represent N6,2′-O-dimethyladenosine (m^6Am), a terminal modification added to the mRNA cap by the methyltransferase PCIF1; m^6Am is a well-established off-target of m^6A antibodies (Fig. 7, B and C) (*43*).

These data support the novel finding that *Kras* is m^6A-methylated at the 3'UTR by METTL3 in the intestinal epithelium.

We next examined how methylation of *Kras* might impact its expression by looking at *Kras* mRNA and KRAS protein levels after METTL3 deletion. Although METTL3 deletion did not significantly impact *Kras* transcript abundance, we observed a substantial decrease in KRAS protein in crypt-enriched lysates from *Mettl3*$^{VilCreER\Delta/\Delta}$ mice compared to controls (Fig. 7, D and E). To further validate our Ribo-seq data *in vivo*, we also examined protein expression levels of other top downregulated genes of interest from the sequencing analysis. This confirmed substantial decreases in YES1 (src family kinase and proto-oncogene) and SEC13 (member of the nuclear pore complex implicated in mRNA export) but not UBE1 (primary enzyme in conjugation of ubiquitin) (*44–46*) (Fig. 7E). Taken together, these data suggest that METTL3 promotes KRAS expression without impacting *Kras* transcript levels, providing further mechanistic support for METTL3 as a post-transcriptional regulator of *Kras*.

We next wanted to confirm that reduced growth factor signaling and KRAS expression were associated with expected functional consequences in METTL3 depleted epithelium. KRAS is a key mediator of epidermal growth factor (EGF) signaling in epithelial cells (*42*). Loss of mitogenic signals such as EGF induces cell cycle arrest and senescence in proliferative cells (*47*). We therefore assessed cellular senescence in inducible *Mettl3*$^{VilCreER\Delta/\Delta}$ epithelium by staining for p21 two days after final tamoxifen injection. As predicted, *Mettl3*$^{VilCreER\Delta/\Delta}$ crypts demonstrated elevated p21 compared to controls, particularly in the upper transit amplifying zone (Fig. 7F). EGF signaling has also been implicated in maintaining genomic integrity in hematopoietic stem cells (*48*). We therefore assessed γ-H2AX levels in inducible *Mettl3*$^{VilCreER\Delta/\Delta}$ crypts at this same early timepoint. As with the p21 staining, inducible *Mettl3*$^{VilCreER\Delta/\Delta}$ mice displayed elevated γ-H2AX staining in the transit amplifying zone (Fig. 7G). One potential caveat to this finding is the possibility of toxic combined effects of CreERT2 and tamoxifen in intestinal stem cells within a week of tamoxifen exposure (*49*). To address this, we injected *Villin-CreERT2* control mice with tamoxifen and examined them at the same timepoint. While we did observe a small number of cells positive for p21 and γ-H2AX in tamoxifen injected *Villin-CreERT2* controls, it was significantly less than seen in *Mettl3*$^{VilCreER\Delta/\Delta}$ mice (fig. S6, A and B). These data suggest that loss of growth factor signaling after METTL3 deletion is associated with cellular senescence and DNA damage in the crypt transit amplifying zone.

Our collective findings examining METTL3 KO in the intestinal epithelium *in vivo* and *in vitro* support a model in which METTL3 methylates the *Kras* transcript and other transcripts involved in growth factor signal transduction. Methylation promotes translation of these transcripts, maintaining responsiveness to extracellular growth factors and thus maintaining proliferation and survival in the transit amplifying cells of the crypt. In the absence of METTL3, loss of growth factor pathway members such as KRAS leads to cellular senescence and genomic instability. Pathological effects of METTL3 deletion manifest strongest in the transit amplifying zone, where rapid proliferation demands the expression of proteins involved in transducing growth factor signals. Loss of transit amplification results in reduced crypt and villus size and diminished production of absorptive cells. (Fig. 8).

Discussion

In this study, we identified an essential role for the m^{6}A methyltransferase, METTL3, in small intestinal epithelial homeostasis. Both constitutive and inducible deletion of METTL3 in the small intestinal epithelium led to death of proliferating transit amplifying cells and collapse of the transit amplifying zone. This was associated with a reduction in villus enterocytes, profound weight loss, and mortality. Transit amplifying cell death accompanied a reduction in translation of transcripts supporting growth factor signaling, including master signaling protein, *Kras*.

Despite their critical role in maintaining homeostatic renewal of the intestinal epithelium, transit amplifying cell dynamics remain poorly understood. We propose that METTL3 is essential for both differentiation and renewal in the transit amplifying zone of the small intestinal crypt. As the site of stem progenitor differentiation, transit amplifying cells are critical to the process of lineage commitment in the cell (*2*). We observed general maintenance of secretory cells adjacent to areas of atrophic crypts in *Mettl3*^{VilCre} and *Mettl3*$^{VilCreER\Delta/\Delta}$ mice. In contrast, these histologically affected areas demonstrated little to no absorptive cell staining. Since mature absorptive cells make up most of the villus surface, transit amplification in the crypt is essential for the production of adequate numbers of absorptive progenitors (*4*). Consistent with our data showing loss of absorptive cells concurrent with loss of transit amplifying cells, a recent study suggested a causal relationship between decreased TA proliferation and an increase in the ratio of secretory to absorptive cells (*50*). Therefore, we propose that METTL3 promotes the production of absorptive cells by maintaining crypt proliferation.

Inducible METTL3 deletion was also associated with a >20 fold increase in the rate of cell death staining in the small intestinal crypt, especially in cells of the TA zone. The rapid proliferation in the transit amplifying zone suggests enhanced dependence on mitogenic factors in these cells. Therefore, the extensive cell death in the transit amplifying cells of *Mettl3*$^{VilCreER\Delta/\Delta}$ mice is consistent with our observation that knockout of METTL3 led to reduced translation of factors implicated in cell survival and proliferation. These transcripts included: growth factor receptor *Fgfr4* (*51*), src family kinase *Yes1* (*44*), guanine nucleotide exchange factor *Tiam1* (*52*), and *Kras*. KRAS is a target of particular interest since a large body of literature has described its critical role in oncogenic pro-proliferative and pro-survival signaling, particularly in the gut (*42*). As much as 50% of colorectal cancers harbor a KRAS mutation (*53*). KRAS binds to guanosine 5'-triphosphate (GTP) in response to extracellular signals such as epidermal growth factor receptor (EGFR) activation. After binding to GTP, KRAS is activated and initiates cell signal transduction pathways such as PI3K-Akt, RAF-MEK-ERK, and upregulation of the GLUT1 glucose transporter (*42*). Although frequently dysregulated in cancer, these pathways are also essential for homeostatic proliferation, differentiation, and survival, and KRAS deletion is incompatible with life in mice (*54*). Numerous studies have implicated METTL3 in the progression of colorectal cancer (*55–57*). In the present manuscript, we provide data in support of a direct homeostatic relationship between METTL3, *Kras* m^{6}A-methylation, and KRAS protein levels. However, it is likely that other factors, in addition to KRAS depletion, underlie the cell death observed in METTL3 depleted transit amplifying cells. We hypothesize that loss of multiple essential components of the growth factor transduction apparatus—including KRAS—overwhelms the cells of the transit amplifying zone and leads to cell death.

We originally hypothesized that METTL3 deletion would have no overt effect on small intestinal epithelial homeostasis based on previous reports that METTL14 was dispensable in the small intestine

(*26*, *27*). Although METTL3 is the catalytic subunit of the m^6A writer complex, seminal studies indicated that METTL14 allosterically activates the METTL3 catalytic site and enhances RNA substrate binding (*24*, *25*). Without METTL14, methylation of RNA substrates *in vitro* was reduced ~90-100%. One possible limitation of these studies is that they were based on methyltransferase activity assays performed in controlled reaction mixtures with synthetic RNA substrates and purified METTL3 and METTL14 protein. These studies do not preclude the possibility of unidentified protein cofactors or variations in RNA primary and secondary structure that might allow METTL3 to maintain some methyltransferase activity in the absence of METTL14. Innumerable studies have deleted METTL14 *in vivo* and *in vitro* and identified residual m^6A on mRNA (*26*, *58*, *59*). Some of this remaining m^6A may be due to the persistence of rRNA, snRNA, or tRNA, which is also m^6A-methylated and often retained after protocols for mRNA enrichment (*60*). Nevertheless, the finding of persistent m^6A after METTL14 deletion raises the possibility of active METTL3 methyltransferase activity in the absence of METTL14. Recent studies identified non-catalytic roles for METTL3 in promoting translation in the cytoplasm of tumor cells (*36*–*38*). However, we found exclusively nuclear staining of METTL3 in ileal enteroids, and we could not rescue death of METTL3 KO enteroids with re-expression of a catalytic inactive form of the protein (fig. S4). Minor delays in enteroid death in METTL3 KO enteroids expressing catalytic inactive METTL3 might imply a role for METTL3 in this tissue outside of its catalytic activity. However, we also observed a small amount of persistent m^6A in mRNA isolated from METTL3 KO enteroids expressing catalytic inactive METTL3 (fig. S4B). We speculate that this persistent m^6A might be the result of catalytic inactive METTL3 delaying the degradation of endogenous METTL3, perhaps by saturating ubiquitination and degradation pathways that target endogenous METTL3. After an additional 24 hours, METTL3 KO enteroids expressing catalytic inactive METTL3 still exhibit near-complete enteroid death (fig. S4E). Taken together, these data strongly suggest that nuclear, catalytic-active METTL3 is required for survival of small intestinal epithelium.

Few studies have compared METTL3 and METTL14 deletion in a single cell type or tissue. Of those, most have supported interdependent roles while few have suggested independent ones. Supporting interdependent roles of METTL3 and METTL14, several studies in cancer cells indicate overlapping functions of these proteins. A study of the colorectal cancer line CT26 found that METTL3 and METTL14 knockout lines exhibited near identical tumorigenicity (*59*). METTL3 and METTL14 deletion had similar effects on growth, self-renewal, and tumorigenesis in glioblastoma stem cells (*61*). Outside of the cancer field, a seminal study in mouse embryonic stem cells compared METTL3 and METTL14 knockout and found equivalent effects on pluripotency (*62*). Additionally, a recent study in murine male germ cells found that deletion of either METTL3 or METTL14 yielded identical effects on fertility (*63*). In terms of substantial divergent roles for METTL3 and METTL14, two recent published studies suggest this possibility in non-transformed cells. In one, neither METTL3 nor METTL14 deletion in the liver effected liver homeostasis; however, METTL14 but not METTL3 deletion negatively impacted liver regeneration after injury. The reason for this discrepancy was not reported (*58*). In another, METTL14 but not METTL3 deletion resulted in reduced pluripotency and self-renewal in mouse embryonic stem cells (*64*). This discrepancy was attributed to non-m^6A roles for METTL14 in chromatin modification.

Our data suggest dramatically divergent roles for METTL3 and METTL14 in homeostatic maintenance of the small intestine. Our findings of deficient proliferation and villus loss in the small intestine contrast strongly with previously published studies demonstrating no substantial role for

METTL14 in the same tissue (*26*, *27*). Our study is somewhat limited by lack of a direct comparison between METTL3 and METTL14 KO intestinal epithelium. Hypothetically, facility-specific differences (e.g., microbiota) could contribute to the discrepancies between our observations in METTL3 KO intestinal epithelium and previously described METTL14 KO intestinal epithelium. However, several factors minimize the possibility of facility or mouse lineage-specific causes for our observed phenotypes. First, mice with intestinal epithelial specific METTL14 KO were described by two separate groups, one in the United States and one in China. Both groups observed colonic disease with no overt small intestinal phenotype, indicating that the METTL14 KO phenotype is likely independent of the mouse housing facility. Second, we tested two different floxed *Mettl3* alleles and two different Cre transgenes in confirming our phenotype, strongly suggesting that METTL3 depletion was directly responsible for the phenotypes we observed rather than indirect effects of the *Cre* transgene or approach to *Mettl3* deletion. Furthermore, *Mettl3*$^{VilCreER\Delta/\Delta}$ enteroids and colonoids recapitulated *in vivo* phenotypes, indicative of an epithelial intrinsic mechanism. Finally, *Mettl3*$^{VilCreER\Delta/\Delta}$ phenotypes persisted even when depleted of their microbiota, suggesting facility-specific microbes did not contribute to our observations. Future studies can therefore examine differences in methylated targets between METTL3 and METTL14 KO small intestinal epithelial cells as an ideal model to identify METTL3 target RNAs that are independent of METTL14 expression.

In summary, our study presents METTL3 as a key regulator of transit amplifying cell dynamics, highlighting RNA modification as a robust, post-transcriptional mechanism contributing to intestinal tissue homeostasis. Furthermore, our unexpected finding of severe small intestinal epithelial defects after METTL3 deletion suggests novel divergent roles for METTL3 independent of METTL14 and underscores the value of examining m^{6}A writer proteins in their native context.

Materials and Methods

Animals

Mettl3$^{VilCre\Delta/\Delta}$ and *Mettl3*$^{VilCreER\Delta/\Delta}$ were generated by crossing *Vil-Cre 1000* mice (JAX #021504) or *Villin-CreERT2* mice (JAX #020282) to previously described *Mettl3*$^{flox/flox}$ mice (*32*) kindly provided by Dr. Richard Flavell at Yale University. *Mettl3*$^{VilCreER\Delta2/\Delta2}$ were generated by crossing *Villin-CreERT2* mice to previously described *Mettl3*$^{flox2/flox2}$ mice (*62*), kindly provided by Dr. Federica Accornero at Ohio State University. For the m^{6}A-seq experiment, wildtype mice were used (JAX #000664). Mouse genotyping was performed by Transnetyx using Taqman qPCR probes. All mice used were C57BL/6J strain. All mouse experiments and handling were approved under IACUC protocol 001278 at the Children's Hospital of Philadelphia. Mice were housed individually in a temperature-controlled room with 12-hour light and dark cycles and continuous access to food and water.

Tamoxifen injection, euthanasia criteria, and survival curves

Tamoxifen injection was initiated in both male and female mice 8-9 weeks old. Mice were injected four times with 50 mg/kg tamoxifen dissolved at 10 mg/mL in corn oil at 24-hour intervals. Mice were weighed at the first injection (this was the starting weight used to calculate subsequent weight change) and then every 48 hours beginning with the day of the final tamoxifen injection. Mice were euthanized once they had

reached humane endpoints defined by the IACUC protocol, which were any of the following: >20% body weight loss, hunched posture, emaciated body condition, or non-responsiveness to stimuli. Survival curves were determined by the number of mice reaching a humane endpoint on each day after tamoxifen injection.

Microbial depletion

Mettl3$^{flox/flox}$ and *Mettl3*$^{VilCreER\Delta/\Delta}$ mice were isolated from the colony at 7 weeks of age and given a cocktail of antibiotics through their drinking water. The antibiotic cocktail was made up of sterile DI water with 0.5g/L of Ampicillin (Sigma A9518), 0.5g/L of Neomycin (MP Biomedicals 180610), 0.5g/L of Gentamicin (Sigma G1914-5G), 0.25g/L of Vancomycin (VWR 0990), 0.25g/L of Metronidazole (Thermo 210340050), and 4g/L Splenda to enhance taste. Mice were weighed daily for the first three days to ensure they were not losing weight due to rejecting the taste of treated water; they were then weighed every 48 hours. After seven days of antibiotic treatment, the mice were injected with tamoxifen for four consecutive days as described above and their stool was collected on the final day of tamoxifen injection to confirm complete elimination of microbiota. Stool from *Mettl3*$^{flox/flox}$ and *Mettl3*$^{VilCreER\Delta/\Delta}$ mice that received only normal drinking water was used as controls. DNA was extracted from stool using the QIAamp Fast DNA Stool Mini Kit (Qiagen 51604) and quantitative PCR was performed using the Applied Biosystems TaqMan Fast Advanced Master Mix (Thermo Scientific 4444556) with TaqMan™ Gene Expression Assay (FAM) primers (Ba04230899_s1) on an Applied Biosystems QuantStudio 3. qPCR data was normalized to stool weight. After confirming microbial depletion, mouse weight was monitored every 48 hours and mice were euthanized according to the criteria described above.

Serum cytokine quantification

Blood was drawn from the inferior vena cava of euthanized mice using a 28G needle, clotted by placing at 25°C for 30 minutes, and then centrifuged at 16,000XG, 25°C for 10 minutes. After centrifugation, serum supernatant was isolated and cytokines were measured using Cytometric Bead Array (BD Biosciences) according to manufacturer's instructions with the following modification: the amount of capture beads, detection reagents, and sample volumes was scaled down tenfold. Data were collected on an LSRFortessa flow cytometer (BD Biosciences) with FACSDiva v9.0 (BD Biosciences) and analyzed with FlowJo v10 (BD Biosciences). Statistical outlier values were removed in GraphPad Prism v9.3 using ROUT method (Q=1%). Cytokine reagents used were mouse TNFα (BD 558299), mouse IL-6 (BD 558301), mouse IL-1α (BD 560157), mouse IL-1β (BD 560232), mouse IL-10 (BD 558300), mouse IL-12/IL-23p40 (BD 560151), and mouse IFN-γ (BD 558296) with the Mouse/Rat Soluble Protein Master Buffer Kit (BD 558266).

Histology and immunofluorescent staining

The large and small intestines were dissected from each mouse and divided into three sections: first half small intestine, second half small intestine, and colon. Each section was flushed with PBS, cut open lengthwise, Swiss-rolled, fixed overnight in 4% paraformaldehyde at 4°C, and then processed for paraffin embedding. Five µm sections from paraffin blocks were mounted on glass slides before deparaffinization

and immunofluorescent staining. Slides were deparaffinized in xylene for one hour, rehydrated in ethanol and then subject to microwave antigen retrieval in either Tris-EDTA pH 9.0 Antigen Retrieval Buffer (10 mM Tris Base, 1 mM EDTA, 0.05% Tween 20, pH 9.0) or Citric Acid pH 6.0 Antigen Retrieval Buffer (Sigma C9999) depending on the target antigen. After antigen retrieval, slides were cooled at room temperature, then blocked in Blocking Buffer (1% BSA and 10% donkey serum in 1x PBS) for an hour at 25°C before primary antibodies were added at 1:200 dilution and incubated overnight at 4°C. The following primary antibodies were used for antigens retrieved in Tris-EDTA pH 9.0 Antigen Retrieval Buffer: Rabbit monoclonal anti-METTL3 (abcam ab195352), Rabbit polyclonal anti-p21 (Proteintech 28248-1-AP), Rabbit monoclonal anti-Phosphorylated-Histone H2A.X (Ser139) (CST 9718), and Rabbit polyclonal anti-SP-1 Chromogranin A (Immunostar 20085). The following primary antibodies were used for antigens retrieved in Citric Acid pH 6.0 Antigen Retrieval Buffer: Rabbit polyclonal anti-LYZ1 (Dako A0099), Rabbit polyclonal anti-MUC2 (Genetex GTX100664), and Rabbit monoclonal anti-Ki67 (abcam ab16667). Goat polyclonal anti-E-Cadherin (R&D Systems AF748) was used alongside all antibodies with both antigen retrieval methods. Slides were washed in 1x PBS before application of secondary antibodies at 1:600 dilution. Secondary antibodies used were Alexa Fluor 488 AffiniPure Bovine Anti-goat IgG (Jackson 805-545-180) or Cy3 AffiniPure Donkey Anti-Rabbit IgG (Jackson 711-165-152). Slides were then washed in 1X PBS and nuclei were counterstained with 1:10,000 DAPI in 1X PBS for 10 minutes. After an additional wash in 1X PBS, slides were dried and coverslips mounted using Prolong Gold Antifade Reagent (CST 9071S). All stains were imaged on the Keyence BZ-X100. Duodenum, jejunum, and ileum were defined as the proximal, middle, and distal third of the small intestine. Proximal colon was defined as the proximal 4 cm of the large intestine, and distal colon as the distal 4 cm of the large intestine.

Non-immunofluorescent staining

For alkaline phosphatase staining: slides were de-paraffinized as described above and stained without antigen retrieval using the Vector® Red Substrate Kit, Alkaline Phosphatase (Vector Laboratories SK-5100) as described in manufacturer's protocol. Slides were counterstained with 1:10,000 DAPI and coverslips mounted with Prolong® Gold Antifade Reagent. For Alcian blue staining: de-paraffinized slides were incubated in mordant in acetic acid 3% aqueous for 3 minutes followed by 1% Alcian blue in 3% acetic acid for 30 minutes, rinsed in water, and counterstained with 0.1% Nuclear Fast Red for 40 seconds, rinsed in water, dehydrated in ethanol followed by xylene, and then coverslip mounted. For TUNEL staining, deparaffinized slides were stained using the Click-iT™ Plus TUNEL Assay for In Situ Apoptosis Detection, Alexa Fluor™ 594 dye (Thermo Scientific C10618) with the following modifications. Slides were washed once in 1X PBS with 0.1% Triton-X100, once in 1X PBS, then the standard protocol was followed beginning at the Proteinase K step. Slides were counterstained with 1:10,000 DAPI and coverslips mounted with Prolong® Gold Antifade Reagent. All stains were imaged on the Keyence BZ-X100.

Histopathology and appearance scoring

Histopathological scoring was performed by a blinded anatomical pathologist at the Children's Hospital of Philadelphia, Dr. Benjamin J. Wilkins. Tissue was scored based on previously published criteria (table S1)

(*65*), with an additional score for villus damage, when scoring small intestine, with criteria as follows: 0 = no change in villus height, 1 = 25% reduction in villus height, 2 = 50% reduction in villus height, 3 = 75% reduction in villus height, 4 = complete loss of villus. For inflammation, extent, regeneration, crypt damage, and villus damage, we scored the most severe finding. For percent involvement, we scored the amount of bowel that was involved by any of the scored processes. Scores were summed for each mouse to generate a separate composite score for small intestine and colon. Mouse appearance/behavior was scored according to a previously described rubric (*66*). In brief, mice were scored on numeric scales for appearance, natural behavior, provoked behavior, and body condition and then scores were summed and reported for each mouse.

Isolation of intestinal crypts

Intestinal sections were dissected, splayed open, rinsed in 1X PBS, and rotated at 4°C for 45 minutes in Hank's Buffered Saline Solution supplemented with 10 mM EDTA and 1 mM N-Acetyl-L-cysteine (Sigma A9165). Crypts were then isolated by scraping with a glass coverslip followed by vortexing and filtering through a 70 uM cell strainer (small intestine) or 100 uM cell strainer (colon). The resulting crypt-enriched suspension was centrifuged at 500xG, 25°C for 5 minutes, washed once in 1X PBS, and pelleted again at 500xG, 25°C for 5 minutes. Supernatant was aspirated and crypt pellets were then applied toward downstream assays.

Intestinal epithelial organoid cultures

Intestinal crypts were isolated as described in the previous section. Duodenum, jejunum, and ileum were defined as the proximal, middle, and distal third of the small intestine. Proximal colon was defined as the proximal 4 cm of the large intestine, and distal colon as the distal 4 cm of the large intestine. Crypts were then washed in 1X sterile PBS three times and plated in Matrigel droplets (Corning 354234). Unless stated otherwise, small intestinal epithelial cultures were overlaid with the following "ENR" medium: advanced DMEM/F12 media (Thermo 12634028) containing 1X GlutaMAX (Thermo 35050061), 10 mM HEPES (Thermo 15-630-080), 1X Antibiotic Antimycotic (Thermo 15240062), 1X N-2 Supplement (Thermo 17502048), 1X B-27 Supplement (Thermo 17504044), 5 µM CHIR99021 (Cayman 13122), 1 mM N-Acetyl-L-cysteine (Sigma A9165), 50 ng/mL mEGF (PeproTech 315-09), 5% Noggin/R-spondin conditioned medium (generated using protocol from (*34*)), and 10 µM Y-27632 (LC Labs Y-5301). Enteroids were fed the same media but without Y-27632 the day after initial plating and every subsequent feeding after that unless otherwise noted. Colonic epithelial cultures were fed 50% WRN CM media (*67*). Enteroids and colonoids were passaged by mechanical dissociation using a P1000 pipette tip attached to a filter-less P200 pipette tip, maintained up to fifteen passages, and passage-matched enteroids and colonoids were used for all experiments. For induction of CreERT2, enteroids and colonoids were fed 1 µM 4-OHT dissolved in 100% ethanol at 48 and 24 hours before beginning of the time course then mechanically passaged at day 0.

Whole mount staining in enteroids

After 48 hours of 4-OHT treatment as described above, *Villin-CreERT2* and *Mettl3*$^{VilCreER\Delta/\Delta}$ enteroids were dissociated to single cells using Accutase (STEMCELL Technologies 07920) for 20 minutes at 37°C. Digested enteroids were resuspended in ENR supplemented with 10 µM Y-27632 and plated on chamber slides pretreated with 10% Matrigel in Advanced DMEM/F12 for 30 minutes at 37°C. After overnight growth as monolayers on chamber slides, enteroids were incubated in 4% PFA at room temperature for 20 minutes, washed three times in 1X PBS, blocked in 10% goat serum in 1X PBS for 30 minutes at 25°C, incubated with 1:200 rabbit monoclonal anti-METTL3 (abcam ab195352) and 1:200 goat polyclonal anti-E-Cadherin (R&D Systems AF748) at 37°C for 30 minutes, washed three times in 1X PBS, incubated with 1:600 Alexa Fluor 488 AffiniPure Bovine Anti-goat IgG (Jackson 805-545-180) and Cy3 AffiniPure Donkey Anti-Rabbit IgG (Jackson 711-165-152) in 1X PBS supplemented with 1:5000 DAPI for 20 min at 25°C, and washed two times in 1X PBS. Finally, chambers were detached from the chamber slide and coverslips mounted with Prolong® Gold Antifade Reagent, and stains were imaged on the Keyence BZ-X100.

qRT-PCR

RNA was isolated using the Quick-RNA Miniprep Kit (Zymo R1054). RNA was reverse transcribed using MultiScribe™ Reverse Transcriptase (Thermo Scientific 4311235) with random hexamer primers. Quantitative PCR was performed using the Applied Biosystems TaqMan Fast Advanced Master Mix (Thermo Scientific 4444556) with TaqMan™ Gene Expression Assay (FAM) primers on an Applied Biosystems QuantStudio 3. The primers used were: *Actin* (Mm02619580_g1), *Olfm4* (Mm01320260_m1), *Bmi1* (Mm03053308_g1), *Clu* (Mm01197002_m1), *Lgr5* (Mm00438890_m1), *Ascl2* (Mm01268891_g1), *Cd44* (Mm01277161_m1), *Hopx* (Mm00558630_m1), and *Kras* (Mm00517494_m1). For determination of relative transcript abundance, the Ct value for *Actin* was subtracted from the Ct value for the gene of interest to obtain *Actin*-normalized ΔCt values, *Actin*-normalized ΔCt values for all control samples were averaged and then the average control *Actin*-normalized ΔCt value was subtracted from the *Actin*-normalized ΔCt value for each individual sample to obtain the ΔΔCt for each sample. Fold change was obtained by raising $2^{-\Delta\Delta Ct}$.

Western blotting

Cells were lysed using RIPA buffer (CST 9806S) supplemented with 1:100 protease phosphatase inhibitor (CST 5872S). Lysates were then passed through a 27G needle five times, incubated on ice for 10 minutes, and then centrifuged at 10,000xG, 4°C for 10 minutes. Protein concentration was measured and normalized using the Pierce™ BCA Protein Assay Kit (Thermo 23225). Lysates were then boiled for 5 minutes with 100 mM DTT and 1X LDS buffer (GenScript M00676) and run on NuPAGE 4-12% Bis-Tris gels (Thermo NP0335BOX) in 1X MOPS-SDS buffer for most proteins (BioWorld 10530007-2) or 1X MES-SDS buffer for proteins below MW ~30 kDa (Thermo NP0002). Proteins were then transferred onto PVDF transfer membrane in 2X NuPAGE transfer buffer (Thermo NP006) on a BioRad semi-dry transfer system. Membranes were then blocked for 1 hr in 5% milk in TBS-T (1X TBS, 0.1% Tween-20), and then placed in 1:1000 primary antibody overnight in 5% milk in TBS-T at 4°C. Blots were then washed three times in TBS-T, and placed in 1:2000 anti-rabbit HRP secondary (CST 7074) or anti-mouse HRP secondary (Novus NBP1-75249) for 1-2 hours at 25°C, and then washed three times in TBS-T again before exposure with

Supersignal® West Femto Maximum Sensitivity Chemiluminescent Substrate on the Biorad Gel Doc XR. Primary antibodies used were mouse anti-beta-Actin (Sigma A5316), rabbit anti-METTL3 (Abcam ab195352), rabbit anti-METTL14 (Sigma HPA038002), rabbit anti-UBE1 (Proteintech 15912-1-AP), rabbit anti-SEC13 (Proteintech 15397-1-AP), mouse anti-c-Yes (Santa Cruz sc-8403), and rabbit anti-KRAS (Proteintech 12063-1-AP).

m^6A dot blot

mRNA was isolated using the Dynabeads™ mRNA DIRECT™ Purification Kit (Thermo 61011). >30 ng of mRNA was heated to 65°C for 2 minutes, placed on ice for >5 minutes, and then pipetted onto a Hybond N+ nitrocellulose membrane and exposed to 254 nm UV light for 5 minutes. The nitrocellulose membrane was then washed in TBS-T (1X TBS, 0.1% Tween-20). Blocked for 1 hr in 5% milk in TBS-T, and then placed in anti m^6A antibody (CST 56593) in 5% BSA overnight at 4°C. Blots were then washed in TBS-T, placed in 1:2000 anti-rabbit HRP secondary for 1-2 hours at 25°C, and then washed in TBS-T again before exposure with Supersignal® West Femto Maximum Sensitivity Chemiluminescent Substrate on the Biorad Gel Doc XR. Total blotted mRNA was stained using 0.04% Methylene Blue (LabChem LC168508) in 0.5M sodium acetate.

RNA-seq and Ribo-seq

Ileal enteroids were expanded in Matrigel in 50% WRN media until approximately 8 to 10 million cells per replicate was achieved. For each genotype, passage separated replicates from the same enteroid line were used. Media was supplemented with 2 uM 4-OHT 72 hours prior to collection. Enteroids were collected by mechanical dissociation, pelleted for 5 seconds on a tabletop mini centrifuge, washed in 1X PBS, pelleted 5 seconds again, and snap frozen in liquid nitrogen. Frozen enteroid pellets were resuspended in ice-cold lysis buffer containing 20mM Tris-HCl pH 7.4, 150mM MgCl2, 150mM NaCl, 100ug/ml cycloheximide, 1% v/v Triton X-100, 1mM DTT, 1U/ul SUPERase·IN RNase inhibitor (ThermoFisher), 25U/ml Turbo DNase1 (ThermoFisher), and 1X EDTA-free protease inhibitor cocktail (Roche). The cells were then lysed by trituration through a 26-gauge needle 10 times for efficient cell lysis. The samples were then processed, and the libraries were prepared as previously described (*41*) with the following modifications. First, we performed sucrose cushion to pellet the ribosome-associated mRNAs and proceeded with RNAse I digestion (10 U/µl by the Epicentre definition) for 30ug of RNA. The samples were incubated at room temperature for 45 minutes with gentle agitation, and the digestion was quenched by adding 200 units of SUPERase·IN. Then, we directly extracted the ribosome-protected fragments (RPF) using the TRIzol reagent and performed gel size selection of the RPFs of 15-35 nucleotides (nt) in length. Second, we performed rRNA depletion using RiboCop for Human/Mouse/Rat kit (Lexogen). Once the rRNA-depleted RPF fragments were obtained, they were pooled together, and the libraries were prepared. The final library contains a 5' adapter – 4 random bases – insert – 5 random bases – sample barcode – 3' adapter. The randomized bases function as Unique molecular identifiers (UMIs) for deduplication. The multiplexed library was then sequenced on Illumina HiSeq 4000 with PE150 runs (paired-end reading of 150 bases), with a sequencing depth of 60 million raw reads per sample. For each sample, one-tenth (150ul) of the lysate was saved for RNA-seq. For RNA-seq, total RNA was extracted using TRIzol LS

reagent (Ambion) and purified using Quick-RNA Microprep kit (Zymo) following the manufacturer's protocol. Libraries were prepared from total RNA using the Smarter® Stranded Total RNA-Seq Kit v2 - Pico Input Mammalian (Takara Bio 634411) and sequenced on a Novaseq 6000, SP Reagent Kit 1.5 (100 cycles). For computational analysis, the raw sequencing data were demultiplexed, the adaptors were removed using cutadapt (*68*), the contaminant sequences (rRNA and tRNA) were depleted, and the reads were deduplicated (umi_tools dedup). The reads were aligned to all transcripts on the mouse reference chromosomes (Gencode version M31, GRCm39) using Kallisto (*69*). Translation efficiency (TE) was calculated by dividing the TPM in the total RNA library by the TPM in the RPF library for each individual transcript and sample. Pathway enrichment analysis was performed using mouse gene symbols orthology-mapped to the human genome and tested against Gene Ontology Biological Process (GOBP) gene sets with the Molecular Signatures Database (MSigDB).

m^6A-seq

Three wildtype C57BL/6J mice (Jax #000664, 2 male 1 female) aged 8 weeks were used. Intestinal crypts were isolated from the distal half of the small intestine as described above. Isolated crypts were dissociated in 10% FBS in 1X PBS supplemented with 20 µg/mL Liberase TH (Roche 05401135001), and 35 µg/ml DNaseI (Roche 10104159001) for 20 minutes at 37°C with frequent agitation. Cell suspensions were then stained with 1:200 PE-EpCAM (BioLegend 118205), 1:200 FITC-CD45 (BioLegend 103107), and 1:1000 DRAQ7 (Thermo Scientific D15106) on ice for 30 minutes in the dark. Approximately 800K live epithelial cells per mouse were then isolated by flow cytometry by sorting for DRAQ7- CD45- PE+ cells directly into Trizol LS (Ambion 10-296-010) on a FACSJazz Sorter. RNA was isolated from Trizol LS using the Direct-zol RNA Microprep Kit (Zymo R2062). RIP-seq was performed according to the "Refined RIP-seq" protocol for low input material (*70*). In brief, 2 µg anti-m^6A antibody (Synaptic Systems 202 003) was incubated with 30 µL Protein A and 30 µL Protein G beads (Thermo 10001D and 10003D) overnight at 4°C, washed, and incubated with 6 ug total RNA that was previously fragmented to ~300 nt fragments with 10 mM ZnCl2 in 10 mM Tris-HCl for 4 minutes at 70°C (5% of fragmented RNA was set aside as input). After 2 hours immunoprecipitation at 4°C, RNA-bead complexes were washed twice in low-salt IP buffer (50 mM NaCl, 10 mM Tris-HCl, pH 7.5, 0.1% IGEPAL CA-630) and twice in high-salt IP buffer (500 mM NaCl, 10 mM Tris-HCl, pH 7.5, 0.1% IGEPAL CA-630) for 10 min each at 4°C. RNA was eluted from the RNA-bead complexes using the Qiagen RNeasy Plus Micro Kit (Qiagen 74034). The isolated m^6A-enriched RNA was immunoprecipitated a second time using 2 µg of a second anti-m^6A antibody (Abcam ab151230) as described in the steps above. Final cDNA Libraries were prepared from twice immunoprecipitated RNA and fragmented input total RNA using the Smarter® Stranded Total RNA-Seq Kit v2 - Pico Input Mammalian (Takara Bio 634411) and sequenced on a Novaseq 6000, SP Reagent Kit 1.5 (100 cycles). Raw reads were aligned to mm10 (gencode_M23_GRCm38.p6) using STAR aligner (2.7.9a). N6-methyladenosine peaks were identified using exomePeak2 (version 1.2.0), followed by a metagene analysis using the bioconducter packages Guitar_2.10.0 and TxDb.Mmusculus.UCSC.mm10.knownGene_3.10.0.

m^{6}A-RIP-qPCR

For m^{6}A-RIP-qPCR, four *Mettl3*$^{flox/flox}$ and four *Mettl3*$^{VilCreER\Delta/\Delta}$ mice aged 8 weeks were used (2 male, 2 female mice per genotype). Intestinal crypts were isolated from the distal half of the small intestine as described above but without digestion to single cells. Whole crypts were pelleted, resuspended in TRI Reagent (Sigma 93289), and RNA was isolated using the Direct-zol RNA Miniprep Kit (Zymo R2050). Next, 20 µg of total RNA was fragmented and immunoprecipitated twice according to the "Refined RIP-seq protocol" as described above. Twice immunoprecipitated RNA and fragmented input total RNA was reverse transcribed using the High-Capacity cDNA Reverse Transcription Kit (Thermo 4368814) and qPCR was performed as described in the "qRT-PCR" section. Taqman probes were as follows: *Gapdh* (Mm99999915_g1), *Kras 5'UTR* (Mm00517491_m1), *Kras 3'UTR* (Mm00517494_m1). For calculation of m^{6}A enrichment, first we calculated the %input for every target in every RIP sample as 2^-(Ct of target gene in RIP – Ct of target gene in input sample). Then we calculated m^{6}A enrichment relative to *Gapdh* by dividing the %input of the target of interest (e.g. *Kras 3'UTR)* by the %input of *Gapdh* for each sample.

Lentiviral constructs and transduction

For lentiviral infection, enteroids were dissociated to single cells using Accutase (STEMCELL Technologies 07920). Digested enteroids were resuspended in ENR with 1:4 lentivirus solution, TransDux MAX Lentivirus Transduction Enhancer (System Biosciences LV860A-1), and 10 uM Y-27632 and plated as monolayers on Collagen I (Advanced Biomatrix 5010). All lentiviral constructs were generated by VectorBuilder and delivered as prepared virus. The transfer vector for catalytic inactive METTL3 expression contained a CMV-EGFP:T2A:Puro selection cassette and the mPGK promoter upstream of the *Mus musculus Mettl3* ORF edited at positions 1183-1194 from GACCCACCTTGG to GCCCCACCTGCG yielding DPPW -> APPA synonymous mutation in the catalytic site. The "GFP" control vector contained a CMV-mCherry:T2A:Puro selection cassette and the EGFP ORF under control of the CMV promoter. After overnight incubation with lentivirus, the enteroid monolayers were mechanically dissociated and replated as 3-dimensional enteroids in Matrigel and selected for antibiotic resistance genes after an additional 48 hours.

Quantification and statistical analysis

Unless otherwise noted, quantification of immunofluorescent staining was performed using three representative images taken per mouse using a 20X objective. Images were taken in three areas of most severe histological distortion (defined as a high-powered field with greatest changes in crypt and/or villus morphology) in distal half of the small intestine of tested mice. For control mice without histological distortion, three representative sections were chosen from matching regions of the distal half of the small intestine. Quantification was performed by an individual blinded to mouse genotype. Unless otherwise noted, each graphed data point is the mean of three quantified representative images per mouse. P values were calculated with the unpaired parametric Student's t test in GraphPad Prism. P values for survival curves were calculated using the Log-rank Mantel-Cox test in GraphPad Prism.

References

1. L. W. Peterson, D. Artis, Intestinal epithelial cells: Regulators of barrier function and immune homeostasis. *Nat. Rev. Immunol.* **14**, 141–153 (2014).
2. H. Gehart, H. Clevers, Tales from the crypt: new insights into intestinal stem cells. *Nat. Rev. Gastroenterol. Hepatol.* **16**, 19–34 (2019).
3. M. Yousefi, L. Li, C. J. Lengner, Hierarchy and Plasticity in the Intestinal Stem Cell Compartment. *Trends Cell Biol.* **27**, 753–764 (2017).
4. B. Tóth, S. Ben-Moshe, A. Gavish, N. Barkai, S. Itzkovitz, Early commitment and robust differentiation in colonic crypts. *Mol. Syst. Biol.* **13**, 902 (2017).
5. X. Ding, J. Boney-montoya, B. M. Owen, A. L. Bookout, C. Coate, D. J. Mangelsdorf, S. A. Kliewer, Crypt Base Columnar Stem Cells in Small Intestines of Mice Are Radioresistant. *Gastroenterology*. **16**, 387–393 (2012).
6. R. J. Gibson, J. M. Bowen, M. R. B. Inglis, A. G. Cummins, D. M. K. Keefe, Irinotecan causes severe small intestinal damage, as well as colonic damage, in the rat with implanted breast cancer. *J. Gastroenterol. Hepatol.* **18**, 1095–1100 (2003).
7. O. J. Sansom, J. Zabkiewicz, S. M. Bishop, J. Guy, A. Bird, A. R. Clarke, MBD4 deficiency reduces the apoptotic response to DNA-damaging agents in the murine small intestine. *Oncogene*. **22**, 7130–7136 (2003).
8. M. K. Zeman, K. A. Cimprich, Causes and consequences of replication stress. *Nat. Cell Biol.* **16**, 2–9 (2014).
9. N. Shyh-Chang, G. Q. Daley, L. C. Cantley, Stem cell metabolism in tissue development and aging. *Dev.* **140**, 2535–2547 (2013).
10. J. Heijmans, J. F. Van Lidth de Jeude, B. K. Koo, S. L. Rosekrans, M. C. B. Wielenga, M. Van De Wetering, M. Ferrante, A. S. Lee, J. J. M. Onderwater, J. C. Paton, A. W. Paton, A. M. Mommaas, L. L. Kodach, J. C. Hardwick, D. W. Hommes, H. Clevers, V. Muncan, G. R. Van Den Brink, ER Stress Causes Rapid Loss of Intestinal Epithelial Stemness through Activation of the Unfolded Protein Response. *Cell Rep.* **3**, 1128–1139 (2013).
11. J. Voog, D. L. Jones, Stem Cells and the Niche: A Dynamic Duo. *Cell Stem Cell*. **6**, 103–115 (2010).
12. J. H. van Es, M. E. van Gijn, O. Riccio, M. van den Born, M. Vooijs, H. Begthel, M. Cozijnsen, S. Robine, D. J. Winton, F. Radtke, H. Clevers, Notch/gamma-secretase inhibition turns proliferative cells in intestinal crypts and adenomas into goblet cells. *Nature*. **435**, 959–63 (2005).
13. Z. Qi, Y. Li, B. Zhao, C. Xu, Y. Liu, H. Li, B. Zhang, X. Wang, X. Yang, W. Xie, B. Li, J.-D. J. Han, Y.-G. Chen, BMP restricts stemness of intestinal Lgr5+ stem cells by directly suppressing their signature genes. *Nat. Commun.* **8**, 13824 (2017).
14. T. Sato, J. H. van Es, H. J. Snippert, D. E. Stange, R. G. Vries, M. van den Born, N. Barker, N. F. Shroyer, M. van de Wetering, H. Clevers, Paneth cells constitute the niche for Lgr5 stem cells in intestinal crypts. *Nature*. **469**, 415–8 (2011).
15. T. Fevr, S. Robine, D. Louvard, J. Huelsken, Wnt/beta-catenin is essential for intestinal homeostasis and maintenance of intestinal stem cells. *Mol. Cell. Biol.* **27**, 7551–9 (2007).
16. P. Chatterji, P. A. Williams, K. A. Whelan, F. C. Samper, S. F. Andres, L. A. Simon, L. R. Parham, R. Mizuno, E. T. Lundsmith, D. S. Lee, S. Liang, H. S. Wijeratne, S. Marti, L. Chau, V. Giroux, B. J. Wilkins, G. D. Wu, P. Shah, G. G. Tartaglia, K. E. Hamilton, Posttranscriptional regulation of colonic epithelial repair by RNA binding protein IMP1/ IGF2BP1. *EMBO Rep.* **20**, 1–16 (2019).
17. P. Chatterji, K. E. Hamilton, S. Liang, S. F. Andres, H. R. S. Wijeratne, R. Mizuno, L. A. Simon, P. D. Hicks, S. W. Foley, J. R. Pitarresi, A. J. Klein-Szanto, A. T. Mah, L. van Landeghem, B. D. Gregory, C. J. Lengner, B. B. Madison, P. Shah, A. K. Rustgi, The LIN28B–IMP1 post-transcriptional regulon has opposing effects on oncogenic signaling in the intestine. *Genes Dev.* **32**, 1020–1034 (2018).
18. B. Han, S. Yan, S. Wei, J. Xiang, K. Liu, Z. Chen, R. Bai, J. Sheng, Z. Xu, X. Gao, YTHDF1-mediated translation amplifies Wnt-driven intestinal stemness. *EMBO Rep.*, 1–14 (2020).
19. S. Jabs, A. Biton, C. Bécavin, M. A. Nahori, A. Ghozlane, A. Pagliuso, G. Spanò, V. Guérineau, D. Touboul, Q. Giai Gianetto, T. Chaze, M. Matondo, M. A. Dillies, P. Cossart, Impact of the gut microbiota on the m6A epitranscriptome of mouse cecum and liver. *Nat. Commun.* **11**, 1–16 (2020).
20. A. Olazagoitia-Garmendia, L. Zhang, P. Mera, J. K. Godbout, M. Sebastian-Delacruz, I. Garcia-Santisteban, L. M. Mendoza, A. Huerta, I. Irastorza, G. Bhagat, P. H. Green, L. Herrero, D. Serra, J. A. Rodriguez, E. F. Verdu, C. He, J. R. Bilbao, A. Castellanos-Rubio, Gluten-induced RNA methylation changes regulate intestinal inflammation via allele-specific XPO1 translation in epithelial cells. *Gut*. **71**, 68–77 (2022).

21. K. D. Meyer, Y. Saletore, P. Zumbo, O. Elemento, C. E. Mason, S. R. Jaffrey, Comprehensive analysis of mRNA methylation reveals enrichment in 3′ UTRs and near stop codons. *Cell*. **149**, 1635–1646 (2012).
22. D. Dominissini, S. Moshitch-Moshkovitz, S. Schwartz, M. Salmon-Divon, L. Ungar, S. Osenberg, K. Cesarkas, J. Jacob-Hirsch, N. Amariglio, M. Kupiec, R. Sorek, G. Rechavi, Topology of the human and mouse m6A RNA methylomes revealed by m6A-seq. *Nature*. **485**, 201–206 (2012).
23. S. Murakami, S. R. Jaffrey, Hidden codes in mRNA: Control of gene expression by m6A. *Mol. Cell*. **82**, 2236–2251 (2022).
24. P. Wang, K. A. Doxtader, Y. Nam, Structural Basis for Cooperative Function of Mettl3 and Mettl14 Methyltransferases. *Mol. Cell*. **63**, 306–317 (2016).
25. X. Wang, J. Feng, Y. Xue, Z. Guan, D. Zhang, Z. Liu, Z. Gong, Q. Wang, J. Huang, C. Tang, T. Zou, P. Yin, Structural basis of N6-adenosine methylation by the METTL3-METTL14 complex. *Nature*. **534**, 575–578 (2016).
26. T. Zhang, C. Ding, H. Chen, J. Zhao, Z. Chen, B. Chen, K. Mao, Y. Hao, M. Roulis, H. Xu, Y. Kluger, Q. Zou, Y. Ye, M. Zhan, R. A. Flavell, H. Li, m6A mRNA modification maintains colonic epithelial cell homeostasis via NF-kB – mediated antiapoptotic pathway. *Sci. Adv.* **5723** (2022).
27. J. Du, R. Sarkar, Y. Li, L. He, W. Kang, W. Liao, W. Liu, T. Nguyen, L. Zhang, Z. Deng, U. Dougherty, S. S. Kupfer, M. Chen, J. Pekow, M. Bissonnette, C. He, Y. C. Li, N6-adenomethylation of GsdmC is essential for Lgr5+ stem cell survival to maintain normal colonic epithelial morphogenesis. *Dev. Cell* (2022), doi:10.1016/j.devcel.2022.07.006.
28. A. Wang, W. Tao, J. Tong, J. Gao, J. Wang, G. Hou, C. Qian, G. Zhang, R. Li, D. Wang, X. Ren, K. Zhang, S. Ding, R. A. Flavell, H. Li, W. Pan, S. Zhu, m6A modifications regulate intestinal immunity and rotavirus infection. *Elife*. **11** (2022), doi:10.7554/eLife.73628.
29. B. B. Madison, L. Dunbar, X. T. Qiao, K. Braunstein, E. Braunstein, D. L. Gumucio, Cis Elements of the Villin Gene Control Expression in Restricted Domains of the Vertical (Crypt) and Horizontal (Duodenum, Cecum) Axes of the Intestine. *J. Biol. Chem.* **277**, 33275–33283 (2002).
30. J. K. Gustafsson, M. E. V. Johansson, The role of goblet cells and mucus in intestinal homeostasis. *Nat. Rev. Gastroenterol. Hepatol.* **19**, 785–803 (2022).
31. C. Wallaeys, N. Garcia-Gonzalez, C. Libert, Paneth cells as the cornerstones of intestinal and organismal health: a primer. *EMBO Mol. Med.*, 1–26 (2022).
32. H.-B. Li, J. Tong, S. Zhu, P. J. Batista, E. E. Duffy, J. Zhao, W. Bailis, G. Cao, L. Kroehling, Y. Chen, G. Wang, J. P. Broughton, Y. G. Chen, Y. Kluger, M. D. Simon, H. Y. Chang, Z. Yin, R. A. Flavell, m6A mRNA methylation controls T cell homeostasis by targeting the IL-7/STAT5/SOCS pathways. *Nature*. **548**, 338–342 (2017).
33. F. El Marjou, K. P. Janssen, B. H. J. Chang, M. Li, V. Hindie, L. Chan, D. Louvard, P. Chambon, D. Metzger, S. Robine, Tissue-specific and inducible Cre-mediated recombination in the gut epithelium. *Genes. (United States)*. **39**, 186–193 (2004).
34. T. Sato, R. G. Vries, H. J. Snippert, M. Van De Wetering, N. Barker, D. E. Stange, J. H. Van Es, A. Abo, P. Kujala, P. J. Peters, H. Clevers, Single Lgr5 stem cells build crypt-villus structures in vitro without a mesenchymal niche. *Nature*. **459**, 262–265 (2009).
35. M. J. Clancy, M. E. Shambaugh, C. S. Timpte, J. A. Bokar, Induction of sporulation in Saccharomyces cerevisiae leads to the formation of N6-methyladenosine in mRNA: A potential mechanism for the activity of the IME4 gene. *Nucleic Acids Res.* **30**, 4509–4518 (2002).
36. S. Lin, J. Choe, P. Du, R. Triboulet, R. I. Gregory, The m6A Methyltransferase METTL3 Promotes Translation in Human Cancer Cells. *Mol. Cell*. **62**, 335–345 (2016).
37. J. Choe, S. Lin, W. Zhang, Q. Liu, L. Wang, J. Ramirez-Moya, P. Du, W. Kim, S. Tang, P. Sliz, P. Santisteban, R. E. George, W. G. Richards, K. K. Wong, N. Locker, F. J. Slack, R. I. Gregory, mRNA circularization by METTL3–eIF3h enhances translation and promotes oncogenesis. *Nature*. **561**, 556–560 (2018).
38. X. Wei, Y. Huo, J. Pi, Y. Gao, S. Rao, M. He, Q. Wei, P. Song, Y. Chen, D. Lu, W. Song, J. Liang, lingjie Xu, H. Wang, G. Hong, Y. Guo, Y. Si, J. Xu, X. Wang, Y. Ma, S. Yu, D. Zou, J. Jin, F. Wang, J. Yu, METTL3 preferentially enhances non-m6A translation of epigenetic factors and promotes tumourigenesis. *Nat. Cell Biol.* **24**, 1278–1290 (2022).
39. S. Zaccara, S. R. Jaffrey, A Unified Model for the Function of YTHDF Proteins in Regulating m6A-Modified mRNA. *Cell*. **181**, 1582-1595.e18 (2020).
40. K. D. Meyer, D. P. Patil, J. Zhou, A. Zinoviev, M. A. Skabkin, O. Elemento, T. V. Pestova, S.-B. Qian, S. R. Jaffrey, 5′ UTR m6A Promotes Cap-Independent Translation. *Cell*. **163**, 999–1010 (2015).
41. A. L. Cope, S. Vellappan, J. S. Favate, K. S. Skalenko, S. S. Yadavalli, P. Shah, Exploring Ribosome-Positioning on Translating Transcripts with Ribosome Profiling. *Methods Mol. Biol.* **2404**, 83–110 (2022).

42. C. Ternet, C. Kiel, Signaling pathways in intestinal homeostasis and colorectal cancer: KRAS at centre stage. *Cell Commun. Signal.* **19**, 1–22 (2021).
43. J. Liu, K. Li, J. Cai, M. Zhang, X. Zhang, X. Xiong, H. Meng, X. Xu, Z. Huang, J. Peng, J. Fan, C. Yi, Landscape and Regulation of m6A and m6Am Methylome across Human and Mouse Tissues. *Mol. Cell*. **77**, 426-440.e6 (2020).
44. I. Garmendia, E. Redin, L. M. Montuenga, A. Calvo, YES1: A Novel Therapeutic Target and Biomarker in Cancer. *Mol. Cancer Ther.* **21**, 1371–1380 (2022).
45. X. Niu, J. Hong, X. Zheng, D. B. Melville, E. W. Knapik, A. Meng, J. Peng, The nuclear pore complex function of sec13 protein is required for cell survival during retinal development. *J. Biol. Chem.* **289**, 11971–11985 (2014).
46. E. J. N. Groen, T. H. Gillingwater, UBA1: At the Crossroads of Ubiquitin Homeostasis and Neurodegeneration. *Trends Mol. Med.* **21**, 622–632 (2015).
47. P. B. Alexander, L. Yuan, P. Yang, T. Sun, R. Chen, H. Xiang, J. Chen, H. Wu, D. R. Radiloff, X.-F. Wang, EGF promotes mammalian cell growth by suppressing cellular senescence. *Cell Res.* **25**, 135–8 (2015).
48. T. Fang, Y. Zhang, V. Y. Chang, M. Roos, C. M. Termini, L. Signaevskaia, M. Quarmyne, P. K. Lin, A. Pang, J. Kan, X. Yan, A. Javier, K. Pohl, L. Zhao, P. Scott, H. A. Himburg, J. P. Chute, Epidermal growth factor receptor-dependent DNA repair promotes murine and human hematopoietic regeneration. *Blood*. **136**, 441–454 (2020).
49. N. Bohin, E. A. Carlson, L. C. Samuelson, Genome Toxicity and Impaired Stem Cell Function after Conditional Activation of CreER T2 in the Intestine. *Stem Cell Reports*. **11**, 1337–1346 (2018).
50. L. E. Sanman, I. W. Chen, J. M. Bieber, V. Steri, C. Trentesaux, B. Hann, O. D. Klein, L. F. Wu, S. J. Altschuler, Transit-Amplifying Cells Coordinate Changes in Intestinal Epithelial Cell-Type Composition. *Dev. Cell*. **56**, 356-365.e9 (2021).
51. Y. Liu, M. Cao, Y. Cai, X. Li, C. Zhao, R. Cui, Dissecting the Role of the FGF19-FGFR4 Signaling Pathway in Cancer Development and Progression. *Front. Cell Dev. Biol.* **8**, 1–9 (2020).
52. P. Boissier, U. Huynh-Do, The guanine nucleotide exchange factor Tiam1: A Janus-faced molecule in cellular signaling. *Cell. Signal.* **26**, 483–491 (2014).
53. M. Peeters, G. Kafatos, A. Taylor, V. M. Gastanaga, K. S. Oliner, G. Hechmati, J.-H. Terwey, J. H. van Krieken, Prevalence of RAS mutations and individual variation patterns among patients with metastatic colorectal cancer: A pooled analysis of randomised controlled trials. *Eur. J. Cancer*. **51**, 1704–13 (2015).
54. L. Johnson, D. Greenbaum, K. Cichowski, K. Mercer, E. Murphy, E. Schmitt, R. T. Bronson, H. Umanoff, W. Edelmann, R. Kucherlapati, T. Jacks, K-ras is an essential gene in the mouse with partial functional overlap with N-ras. *Genes Dev.* **11**, 2468–2481 (1997).
55. J. Pan, F. Liu, X. Xiao, R. Xu, L. Dai, M. Zhu, H. Xu, Y. Xu, A. Zhao, W. Zhou, Y. Dang, G. Ji, METTL3 promotes colorectal carcinoma progression by regulating the m6A–CRB3–Hippo axis. *J. Exp. Clin. Cancer Res.* **41**, 1–17 (2022).
56. H. Chen, S. Gao, W. Liu, C. C. Wong, J. Wu, J. Wu, D. Liu, H. Gou, W. Kang, J. Zhai, C. Li, H. Su, S. Wang, F. Soares, J. Han, H. H. He, J. Yu, RNA N6-Methyladenosine Methyltransferase METTL3 Facilitates Colorectal Cancer by Activating the m6A-GLUT1-mTORC1 Axis and Is a Therapeutic Target. *Gastroenterology*. **160**, 1284-1300.e16 (2021).
57. T. Li, P. S. Hu, Z. Zuo, J. F. Lin, X. Li, Q. N. Wu, Z. H. Chen, Z. L. Zeng, F. Wang, J. Zheng, D. Chen, B. Li, T. B. Kang, D. Xie, D. Lin, H. Q. Ju, R. H. Xu, METTL3 facilitates tumor progression via an m6A-IGF2BP2-dependent mechanism in colorectal carcinoma. *Mol. Cancer*. **18**, 1–15 (2019).
58. X. Cao, Y. Shu, Y. Chen, Q. Xu, G. Guo, Z. Wu, M. Shao, Y. Zhou, M. Chen, Y. Gong, C. Li, Y. Shi, H. Bu, Mettl14-Mediated m6A Modification Facilitates Liver Regeneration by Maintaining Endoplasmic Reticulum Homeostasis. *Cmgh*. **12**, 633–651 (2021).
59. L. Wang, H. Hui, K. Agrawal, Y. Kang, N. Li, R. Tang, J. Yuan, T. M. Rana, m 6 A RNA methyltransferases METTL3/14 regulate immune responses to anti-PD-1 therapy . *EMBO J.* **39**, 1–15 (2020).
60. C. Legrand, F. Tuorto, M. Hartmann, R. Liebers, D. Jacob, M. Helm, F. Lyko, Statistically robust methylation calling for wholetranscriptome bisulfite sequencing reveals distinct methylation patterns for mouse RNAs. *Genome Res.* **27**, 1589–1596 (2017).
61. Q. Cui, H. Shi, P. Ye, L. Li, Q. Qu, G. Sun, G. Sun, Z. Lu, Y. Huang, C. G. Yang, A. D. Riggs, C. He, Y. Shi, m6A RNA Methylation Regulates the Self-Renewal and Tumorigenesis of Glioblastoma Stem Cells. *Cell Rep.* **18**, 2622–2634 (2017).
62. J. H. H. Shay Geula, Sharon Moshitch-Moshkovitz, Dan Dominissini, Abed AlFatah Mansour, Nitzan Kol, Mali Salmon-Divon, Vera Hershkovitz, Eyal Peer, Nofar Mor, Yair S. Manor, Moshe Shay Ben-Haim, Eran Eyal, Sharon Yunger, Yishay Pinto, Diego Adhemar Jaitin, m6A mRNA methylation facilitates resolution of naïve pluripotency toward differentiation. *Science (80-.).* **347**,

1002–1006 (2015).
63. Z. Lin, P. J. Hsu, X. Xing, J. Fang, Z. Lu, Q. Zou, K. J. Zhang, X. Zhang, Y. Zhou, T. Zhang, Y. Zhang, W. Song, G. Jia, X. Yang, C. He, M. H. Tong, Mettl3-/Mettl14-mediated mRNA N 6-methyladenosine modulates murine spermatogenesis. *Cell Res.* **27**, 1216–1230 (2017).
64. X. Dou, L. Huang, Y. Xiao, C. Liu, Y. Li, X. Zhang, L. Yu, R. Zhao, L. Yang, C. Chen, X. Yu, B. Gao, M. Qi, Y. Gao, B. Shen, S. Sun, C. He, J. Liu, METTL14 is a chromatin regulator independent of its RNA N 6 -methyladenosine methyltransferase activity. *Protein Cell*, 1–76 (2023).
65. L. A. Dieleman, M. J. Palmen, H. Akol, E. Bloemena, A. S. Peña, S. G. Meuwissen, E. P. Van Rees, Chronic experimental colitis induced by dextran sulphate sodium (DSS) is characterized by Th1 and Th2 cytokines. *Clin. Exp. Immunol.* **114**, 385–91 (1998).
66. E. V Paster, K. A. Villines, D. L. Hickman, Endpoints for mouse abdominal tumor models: refinement of current criteria. *Comp. Med.* **59**, 234–41 (2009).
67. H. Miyoshi, T. S. Stappenbeck, In vitro expansion and genetic modification of gastrointestinal stem cells in spheroid culture. *Nat. Protoc.* **8**, 2471–2482 (2013).
68. M. Martin, Cutadapt removes adapter sequences from high-throughput sequencing reads. *EMBnet.journal*. **17**, 10 (2011).
69. N. L. Bray, H. Pimentel, P. Melsted, L. Pachter, Near-optimal probabilistic RNA-seq quantification. *Nat. Biotechnol.* **34**, 525–527 (2016).
70. Y. Zeng, S. Wang, S. Gao, F. Soares, M. Ahmed, H. Guo, M. Wang, J. T. Hua, J. Guan, M. F. Moran, M. S. Tsao, H. H. He, Refined RIP-seq protocol for epitranscriptome analysis with low input materials. *PLoS Biol.* **16**, 1–20 (2018).

Acknowledgments

We thank Dr. Richard Flavell (Yale University), Dr. Federica Accornero (Ohio State University), and Dr. Brian Capell (University of Pennsylvania Perelman School of Medicine) for generously providing Mettl3-floxed mice used in this study. For feedback, technical assistance, and/or sharing of laboratory reagents, we thank: Dr. Michael Silverman, Dr. Michael Abt, Dr. Tatiana Karakasheva, Gloria Soto, Dr. Amanda Muir, Dr. Masaru Sasaki, Joshua Wang, Dr. Lan Lin, Dr. Samir Adhikari, Dr. Derek Sung, and Nora Kiledjian (Children's Hospital of Philadelphia/University of Pennsylvania Perelman School of Medicine) and Dr. Igor Brodsky, Dr. Chris Lengner, and Zvi Cramer (University of Pennsylvania School of Veterinary Medicine). We also thank the following scientific cores and centers: The Center for Molecular Studies in Digestive and Liver Diseases (P30DK050306) and the Molecular Pathology and Imaging Core (RRID: SCR_022420), the Flow Cytometry Core at the Children's Hospital of Philadelphia, and the Center for Applied Genomics at the Children's Hospital of Philadelphia. Artwork depicting mouse injection schemes was created with BioRender.com

Funding:
NIH R01-DK124369 (KEH)
NIH R21-ES031533 (KEH)
The Children's Hospital of Philadelphia Institutional Development Funds (KEH)
The Gastrointestinal Epithelium Modeling Program (KEH)

Author contributions:
Conceptualization: CHD, KEH
Methodology: CHD, EAM, SV, PS
Formal analysis: CHD, KEH[2], SV, YZ, BJW
Investigation: CHD, KEN, SV, RM, SKN, KK, LP, XM, AC
Visualization: CHD, KEH[2]
Supervision: CHD, KEH, PS, MDW
Writing—original draft: CHD, KEH
Writing—review & editing: CHD, KEH, KK, MDW

KEH: Katharyn E. Hamilton
KEH[2]: Katharina E. Hayer

Competing interests:
Premal Shah is a member of the Scientific Advisory Board of Trestle Biosciences and is Director at Ananke Therapeutics. All other authors declare they have no competing interests.

Data and materials availability:
All data needed to evaluate the conclusions in the paper are present in the paper and/or the Supplementary Materials.

Figures and Tables

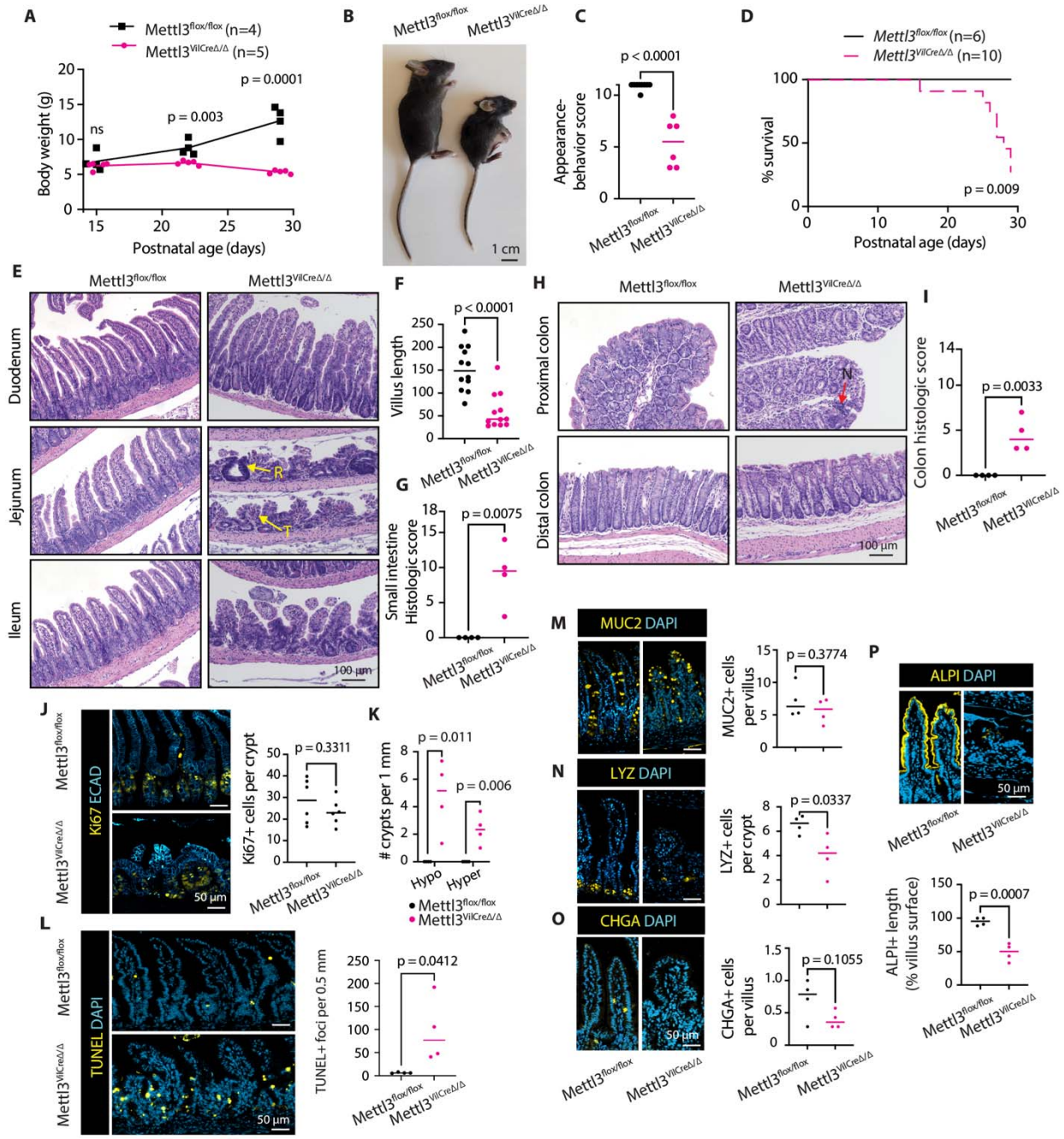

Fig.1. Prenatal intestinal epithelial METTL3 deletion is associated with complete growth retardation and severe small intestinal epithelial distortion. (A) Growth curves of *Mettl3*$^{flox/flox}$ (n=4) and *Mettl3*$^{VilCre\Delta/\Delta}$ (n=5) mice from postnatal day 15 to 29**. (B)** Gross appearance of *Mettl3*$^{flox/flox}$ and *Mettl3*$^{VilCre\Delta/\Delta}$ at 29 days of age. **(C)** Composite appearance and behavior score of *Mettl3*$^{flox/flox}$ (n=9) and *Mettl3*$^{VilCre\Delta/\Delta}$ (n=6) at 29 days of age. **(D)** Kaplan-Meier survival curves of *Mettl3*$^{flox/flox}$ (n=6) and *Mettl3*$^{VilCre\Delta/\Delta}$ (n=10) mice through postnatal day 29; p value corresponds to Log-rank (Mantel-Cox) test. **(E)** Representative H&E stains of duodenum, jejunum, and ileum of *Mettl3*$^{flox/flox}$ and *Mettl3*$^{VilCre\Delta/\Delta}$ mice. "R" indicates regenerative crypt. "T" indicates villus tufting. **(F)** Quantification of shortest villus lengths identified in jejunal sections, n=3 sections each for n=4 *Mettl3*$^{flox/flox}$ and *Mettl3*$^{VilCre\Delta/\Delta}$ mice. **(G)** Composite histological score for small intestine, n=4 *Mettl3*$^{flox/flox}$ and *Mettl3*$^{VilCre\Delta/\Delta}$ mice. **(H)** Representative H&E stains of proximal and distal colon. "N" denotes neutrophil invasion. **(I)** Composite histological score for colon, n=4 *Mettl3*$^{flox/flox}$ and *Mettl3*$^{VilCre\Delta/\Delta}$ mice. **(J)** Representative images and quantification of Ki67 in distal half small intestine of n=6 *Mettl3*$^{flox/flox}$ and *Mettl3*$^{VilCre\Delta/\Delta}$ mice. **(K)** Number of hypo- (<10 Ki67+ cells) or hyper-proliferative (>45 Ki67+ cells) crypts per 1 mm distal half small intestine in n=4 *Mettl3*$^{flox/flox}$ and *Mettl3*$^{VilCre\Delta/\Delta}$ mice. **(L)** Representative images and quantification of TUNEL staining in distal half small intestine of n=4 *Mettl3*$^{flox/flox}$ and *Mettl3*$^{VilCre\Delta/\Delta}$ mice. **(M, N, O)** Representative images and quantification of

intestinal secretory markers MUC2, LYZ, and CHGA in distal half small intestine of n=4 *Mettl3*$^{flox/flox}$ and *Mettl3*$^{VilCre\Delta/\Delta}$ mice. **(P)** Representative images and quantification of alkaline phosphatase staining in distal half small intestine of n=4 *Mettl3*$^{flox/flox}$ and *Mettl3*$^{VilCre\Delta/\Delta}$ mice. Unless otherwise noted, images and quantification from areas of most severe histological distortion in distal half small intestine of 29d old mice. Unless otherwise noted, each data point is the mean of three representative sections imaged per mouse with bar at median value and p denotes value of unpaired parametric Student's t test.

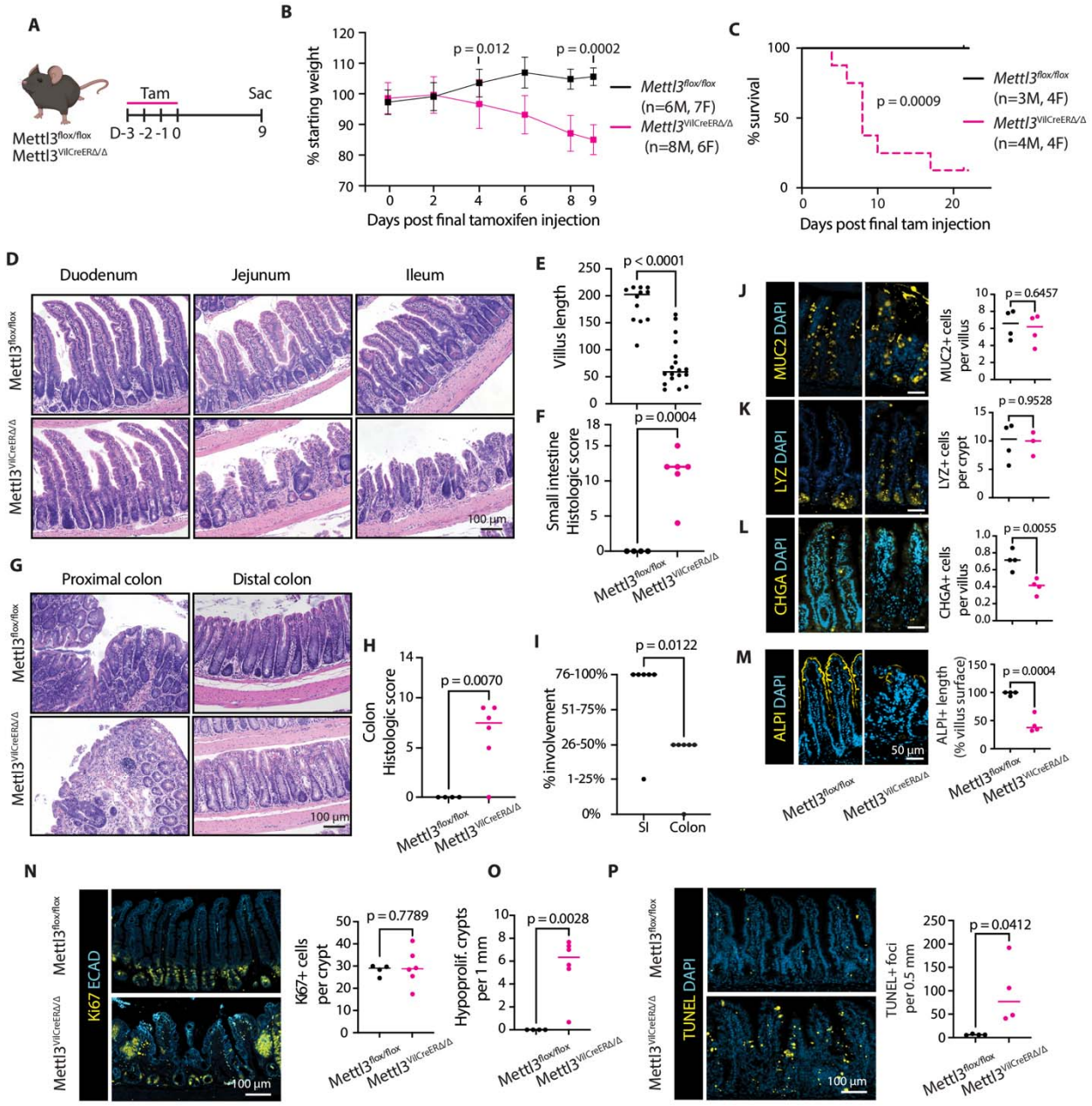

Fig. 2. Intestinal epithelial METTL3 is required for survival and small intestinal epithelial homeostasis in adult mice. (A) Schematic depicting tamoxifen injection and sacrifice scheme for 8-week-old *Mettl3*$^{flox/flox}$ and *Mettl3*$^{VilCreERΔ/Δ}$ mice. **(B)** Weight curves through nine days post tamoxifen injection for *Mettl3*$^{flox/flox}$ (n=13) and *Mettl3*$^{VilCreERΔ/Δ}$ (n=14) mice. Data presented as mean +/- SD **(C)** Kaplain-Meier survival curves of *Mettl3*$^{flox/flox}$ (n=7) and *Mettl3*$^{VilCreERΔ/Δ}$ (n=8) mice after tamoxifen injection, p value corresponds to Log-rank (Mantel-Cox) test. **(D)** Representative H&E stains of duodenum, jejunum, and ileum of *Mettl3*$^{flox/flox}$ and *Mettl3*$^{VilCreERΔ/Δ}$ mice. **(E)** Quantification of shortest villus lengths identified in jejunal sections, n=3 sections each for *Mettl3*$^{flox/flox}$ (n=4) and *Mettl3*$^{VilCreERΔ/Δ}$ (n=6) mice. **(F)** Composite histological score for small intestine in *Mettl3*$^{flox/flox}$ (n=4) and *Mettl3*$^{VilCreERΔ/Δ}$ (n=6) mice. **(G)** Representative H&E stains of proximal and distal colon of *Mettl3*$^{flox/flox}$ and *Mettl3*$^{VilCreERΔ/Δ}$ mice. **(H)** Composite histological score for colon of *Mettl3*$^{flox/flox}$ (n=4) and *Mettl3*$^{VilCreERΔ/Δ}$ (n=6) mice. **(I)** Greatest percent involvement for any criteria comprising histological score depicted in F or H. **(J, K, L)** Representative images and quantification of intestinal secretory markers MUC2, LYZ, and CHGA in distal half small intestine of n=4 *Mettl3*$^{flox/flox}$ and *Mettl3*$^{VilCreERΔ/Δ}$ mice. **(M).** Representative images and quantification of alkaline phosphatase activity in distal half small intestine of n=4 *Mettl3*$^{flox/flox}$ and

Mettl3$^{VilCreER\Delta/\Delta}$ mice. **(N)** Representative images and quantification of Ki67 in distal half small intestine of *Mettl3*$^{flox/flox}$ (n=4) and *Mettl3*$^{VilCreER\Delta/\Delta}$ (n=6) mice. **(O)** Number of hypo-proliferative (<10 Ki67+ cells) crypts per 1 mm intestine corresponding to sections analyzed in (N). **(P)** Representative images and quantification of TUNEL staining in distal half small intestine of n=4 *Mettl3*$^{flox/flox}$ and *Mettl3*$^{VilCreER\Delta/\Delta}$ mice. Unless otherwise noted, images and quantification from areas of most severe histological distortion in distal half small intestine of mice nine days post final tamoxifen injection initiated at 8 weeks of age. Unless otherwise noted, each data point is the mean of three representative sections imaged per mouse with bar at median value and p denotes value of unpaired parametric Student's t test.

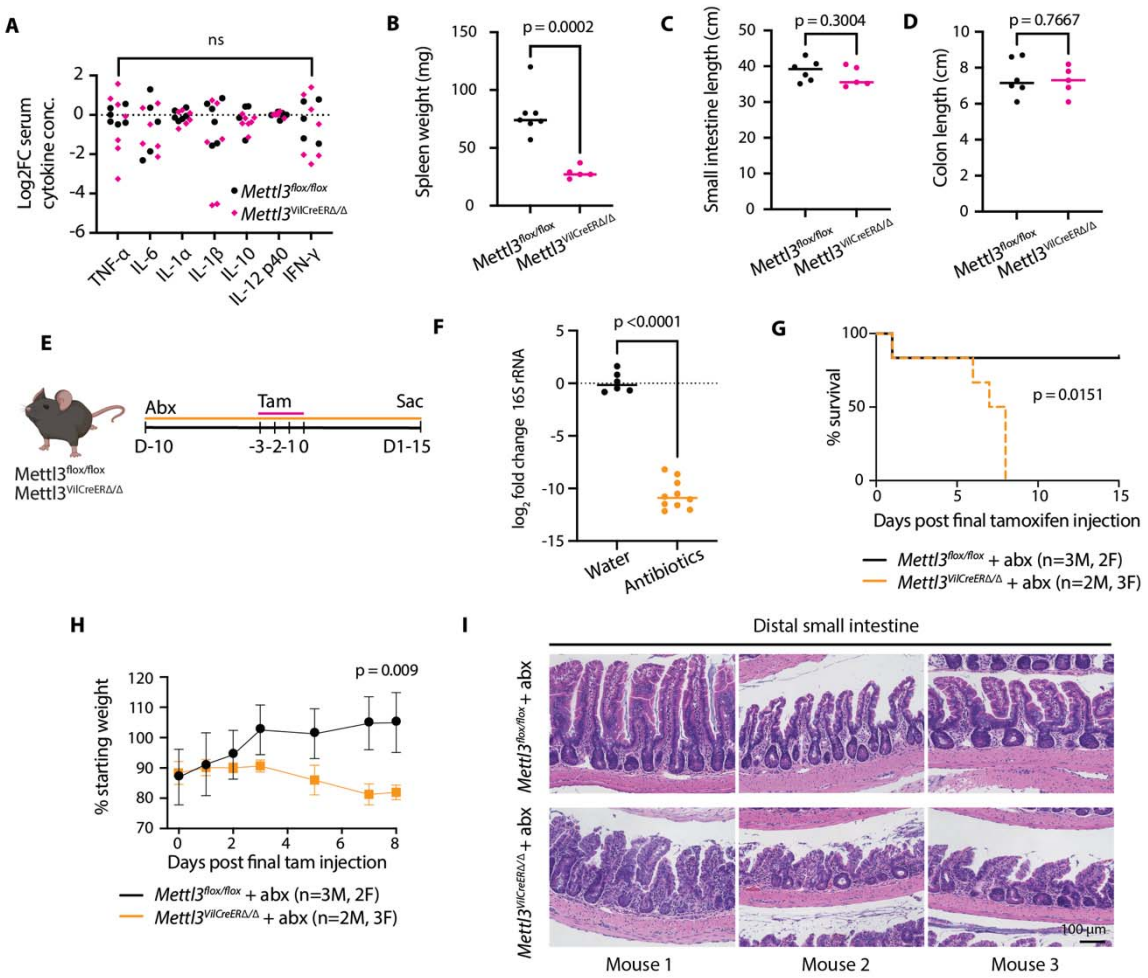

Fig. 3. METTL3 deletion disrupts small intestinal epithelial homeostasis independent of intestinal microbiota. (A) Log_2 fold change in serum cytokines detected by cytometric bead array in *Mettl3*$^{flox/flox}$ (n=6) and *Mettl3*$^{VilCreER\Delta/\Delta}$ (n=7) mice nine days post final tamoxifen injection, ns indicates p > 0.05 for all cytokines measured. **(B)** Spleen weight in *Mettl3*$^{flox/flox}$ (n=7) and *Mettl3*$^{VilCreER\Delta/\Delta}$ (n=5) mice nine days post final tamoxifen injection. **(C)** Small intestine length in *Mettl3*$^{flox/flox}$ (n=6) and *Mettl3*$^{VilCreER\Delta/\Delta}$ (n=5) mice nine days post final tamoxifen injection. **(D)** Colon length in *Mettl3*$^{flox/flox}$ (n=6) and *Mettl3*$^{VilCreER\Delta/\Delta}$ (n=5) mice nine days post final tamoxifen injection. **(E)** Schematic for antibiotic (abx) treatment and tamoxifen injection of mice beginning in 7-week-old mice. **(F)** Log_2 fold change in 16S rRNA amplified from fecal bacterial DNA at the final day of tamoxifen injection in *Mettl3*$^{flox/flox}$ and *Mettl3*$^{VilCreER\Delta/\Delta}$ mice treated with antibiotic (n=10) or control water vehicle (n=6). **(G)** Kaplain-Meier survival curve for *Mettl3*$^{flox/flox}$ (n=5) and *Mettl3*$^{VilCreER\Delta/\Delta}$ (n=5) mice post antibiotic and tamoxifen treatment. **(H)** Weight change post final tamoxifen injection in antibiotic treated *Mettl3*$^{flox/flox}$ (n=5) and *Mettl3*$^{VilCreER\Delta/\Delta}$ (n=5) mice. Data presented as mean +/- SD **(I)** Representative H&E stains from matched sections of distal small intestine in antibiotic treated *Mettl3*$^{flox/flox}$ and *Mettl3*$^{VilCreER\Delta/\Delta}$ mice, each image shown is from a unique mouse. Unless otherwise noted, each data point represents a single mouse with bar at median value and p denotes value of unpaired parametric Student's t test.

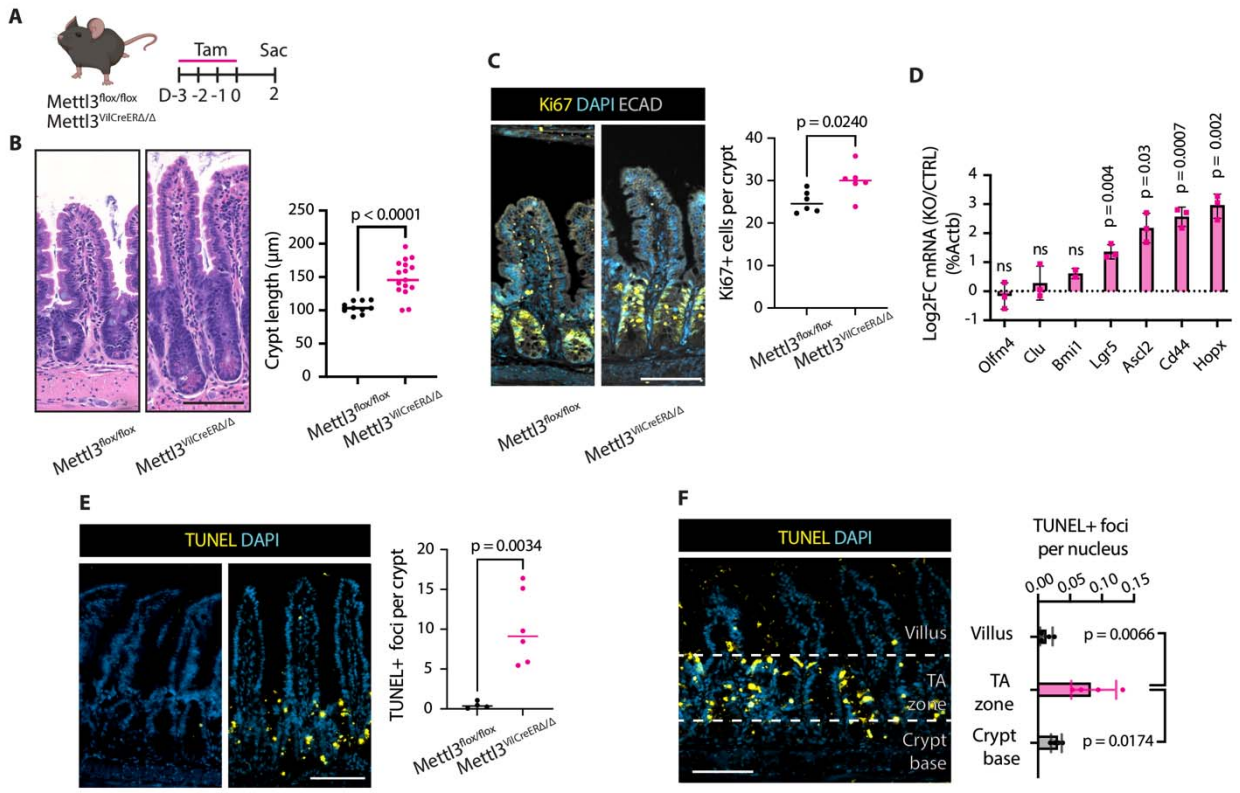

Fig. 4. METTL3 deletion rapidly induces death of proliferative transit amplifying cells. (A) Schematic for tamoxifen injection in 8-week-old *Mettl3*$^{flox/flox}$ and *Mettl3*$^{VilCreER\Delta/\Delta}$ mice followed by sacrifice 48 hours after final injection. **(B)** Representative images and quantification of crypt height in distal half small intestine of *Mettl3*$^{flox/flox}$ (n=5) and *Mettl3*$^{VilCreER\Delta/\Delta}$ (n=8) mice, points represent quantification of n=2 regions of greatest crypt height for each mouse. **(C)** Representative images and quantification of Ki67 staining in distal half small intestine of *Mettl3*$^{flox/flox}$ (n=6) and *Mettl3*$^{VilCreER\Delta/\Delta}$ (n=6) mice. **(D)** Log_2 fold change in qPCR quantification of markers of intestinal stem cells and progenitors normalized to *Actb* and the mean of *Mettl3*$^{flox/flox}$ controls in crypt enriched lysates from distal half small intestine of *Mettl3*$^{flox/flox}$ (n=3) and *Mettl3*$^{VilCreER\Delta/\Delta}$ (n=3) mice. **(E)** Representative images and quantification of TUNEL staining in distal half small intestine *Mettl3*$^{flox/flox}$ (n=4) and *Mettl3*$^{VilCreER\Delta/\Delta}$ (n=6) mice. **(F)** Representative image and quantification of distribution of TUNEL staining in villus, transit amplifying (TA) zone, and crypt base in distal half small intestine of *Mettl3*$^{VilCreER\Delta/\Delta}$ mice (n=4). Images and quantification from areas of most severe histological distortion in distal small intestine of mice two days post final tamoxifen injection. Unless otherwise noted, each data point is the mean of three representative sections imaged per mouse with bar at median value and p denotes value of unpaired parametric Student's t test. Scale bar 100 µM.

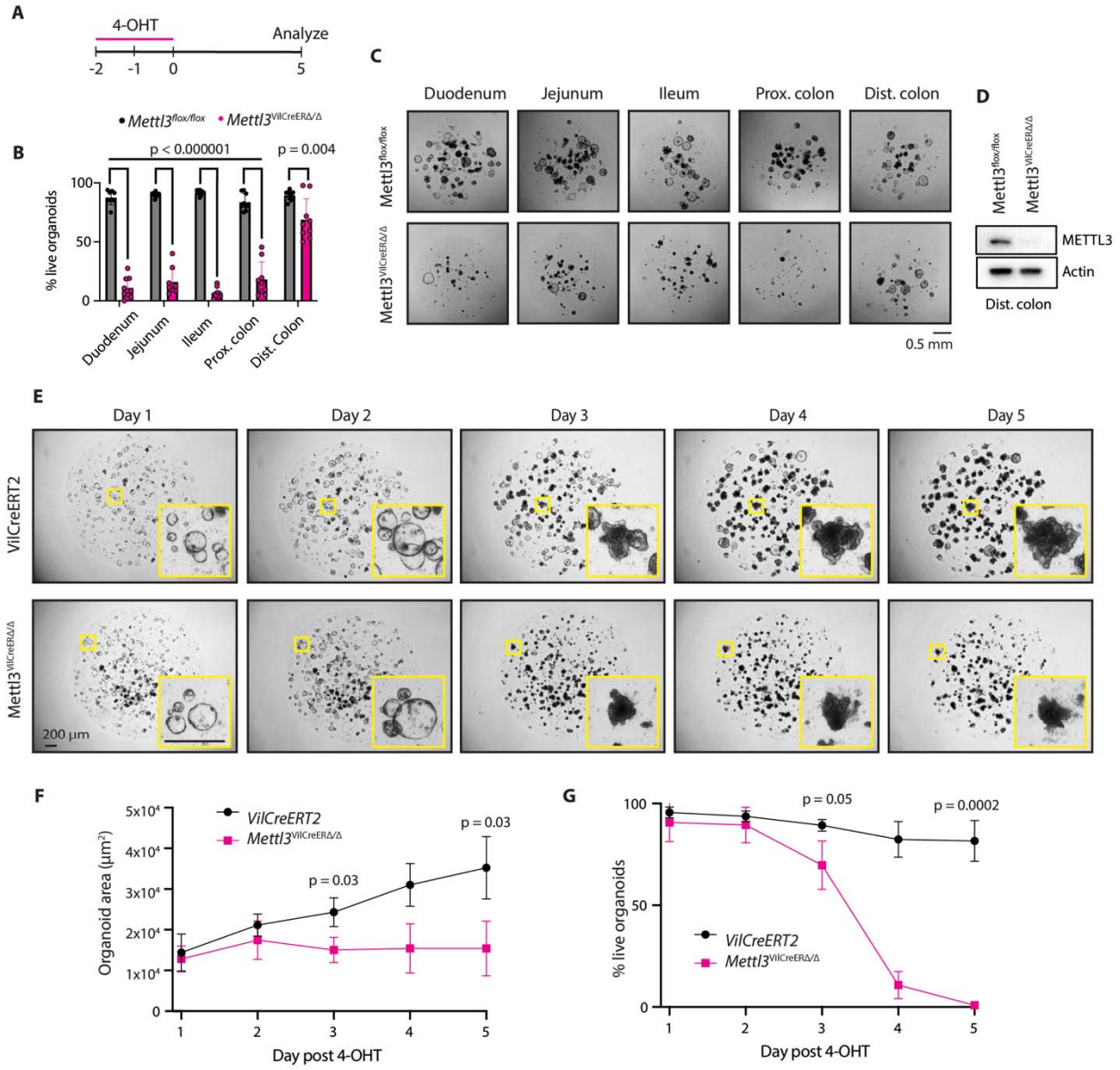

Figure 5. METTL3 deletion triggers growth arrest and death in intestinal epithelial enteroids and colonoids. (A) Intestinal epithelial enteroids or colonoids were treated with 1 µm 4-OHT 48 and 24 hours before beginning of time course and analyzed at days 1 through 5. **(B)** Percent live enteroids or colonoids at 5 days post 4-OHT treatment of enteroids derived from duodenum, jejunum, and ileum, and colonoids derived from proximal or distal colon. Dead enteroids or colonoids were defined as those being completely opaque, spilling luminal debris, and not demonstrating any growth in the subsequent 24 hours. Each point represents n=9 technical replicates across n=3 passage separated biological replicates for each genotype. Bar height at median value with error bars as +/- SD. **(C)** Representative images at 5 days post 4-OHT treatment corresponding to quantification in (B). **(D)** Western blot depicting depletion of METTL3 in surviving *Mettl3*$^{VilCreER\Delta/\Delta}$ distal colonoids six days after 4-OHT treatment. **(E)** Representative images of ileal enteroids at five days post 4-OHT treatment with individual enteroids highlighted in yellow insets. **(F)** ImageJ quantification of average ileal enteroid 2D area at each day post 4-OHT treatment for VillinCreERT2 (VilCreERT2) and *Mettl3*$^{VilCreER\Delta/\Delta}$ enteroids, n=3 passage separated replicates. Data presented as mean +/- SD. P-value represents unpaired parametric Student's t test at day 3 and day 5. **(G)** Percent live ileal enteroids at each day post 4-OHT treatment for VillinCreERT2 (VilCreERT2) and *Mettl3*$^{VilCreER\Delta/\Delta}$ enteroids, n=3 passage separated biological replicates. Dead enteroids were defined as described in (B). Data presented as mean +/- SD. P-value represents unpaired parametric Student's t test at day 3 and day 5.

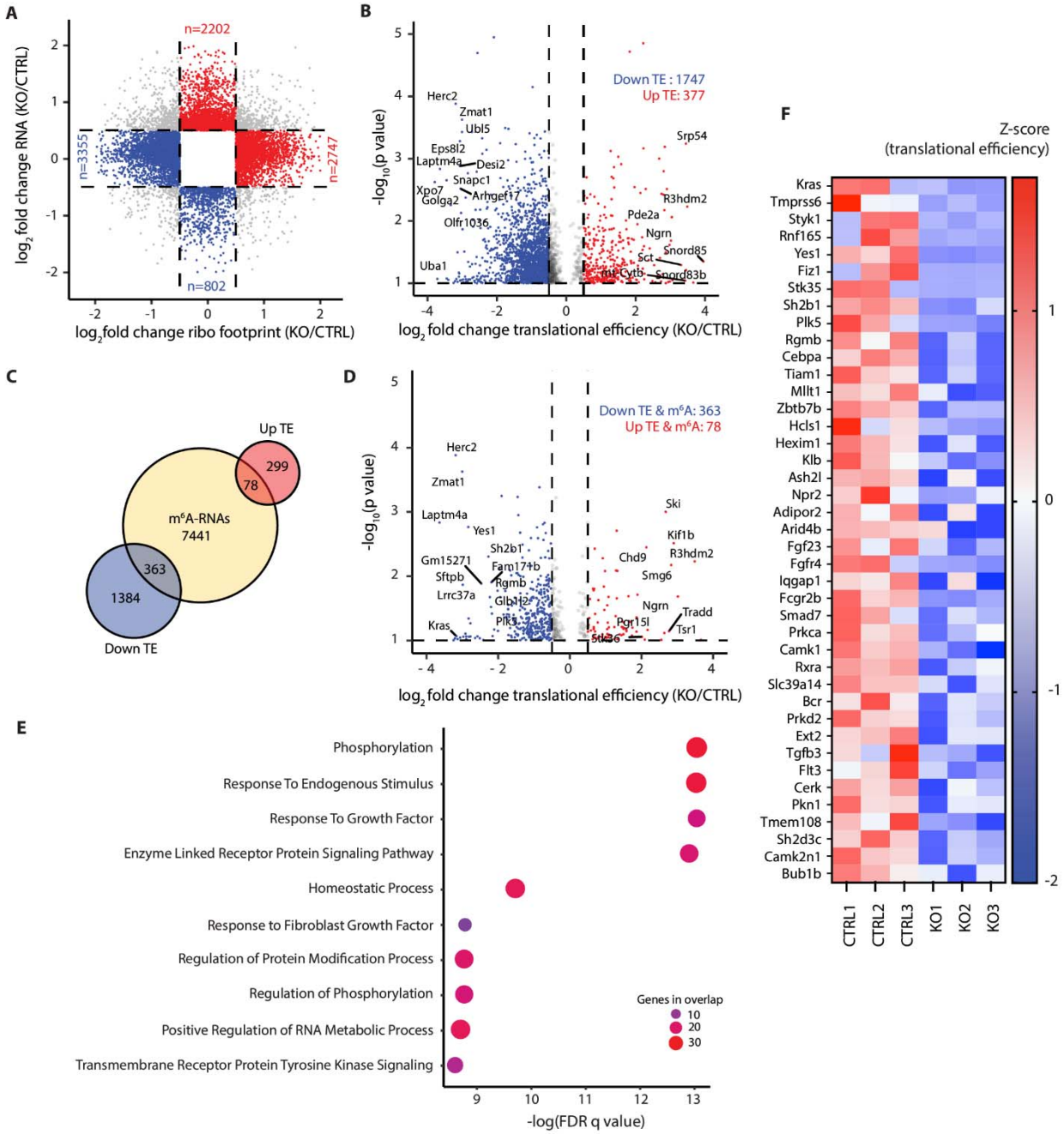

Figure 6. METTL3 deletion leads to a global decrease in mRNA translational efficiency with impacts on growth factor signaling. (A) Scatter plot of log_2 fold change in ribosome footprint and total transcript abundance for all transcripts detected in RNA-seq and Ribo-seq of *Mettl3*$^{flox/flox}$ (CTRL) and *Mettl3*$^{VilCreERΔ/Δ}$ (KO) ileal enteroids 72 hours post initiation of 4-OHT treatment. Log2 fold change cut off >0.5 or <-0.5. Red marks transcripts increased in RNA or ribosome footprint abundance only. Blue marks transcripts decreased in RNA or ribosome footprint abundance only. Grey marks transcripts changed in both. **(B)** Volcano plot of all transcripts with log_2 fold change in translational efficiency (TE) >0.5 or <-0.5 and $-log_{10}$ p value >1. Red marks all transcripts with increased TE and blue marks all transcripts with decreased TE. **(C)** Venn diagram depicting fraction of transcripts with changes in TE and at least one m^{6}A peak as determined by m^{6}A-seq of wildtype mouse small intestinal crypt epithelium. Yellow circle is all m^{6}A-methylated transcripts detected by m^{6}A-seq. Blue circle is all transcripts with decreased TE from (B). Red circle is all transcripts with increased TE from (B). **(D)** Volcano plot of all transcripts displayed in (B), now filtered for transcripts containing at least one m^{6}A peak according to m^{6}A-seq of wildtype mouse small intestinal crypt epithelium. Red marks all transcripts with increased TE and blue marks all transcripts with decreased TE. **(D)** Pathway enrichment analysis comparing transcripts with downregulated TE (log_2FC < -1) and at least one m^{6}A peak against Gene Ontology Biological Process (GOBP) gene sets. Circle color

and size both scale with number of genes overlapping between the tested gene set and the GOBP gene set. **(F)** Heat map depicting Z-scores for TE in three *Mettl3*$^{flox/flox}$ (CTRL) and three *Mettl3*$^{VilCreER\Delta/\Delta}$ (KO) replicates 72 hours post initiation of 4-OHT treatment. Genes presented are all 42 genes from the four most-enriched pathways in (E), *i.e.* highest -log(FDR q value). Genes are presented in order of greatest decrease in mean TE to smallest. All data from RNA-seq and Ribo-seq of *Mettl3*$^{flox/flox}$ (CTRL) and *Mettl3*$^{VilCreER\Delta/\Delta}$ (KO) ileal enteroids 72 hours post initiation of 4-OHT treatment.

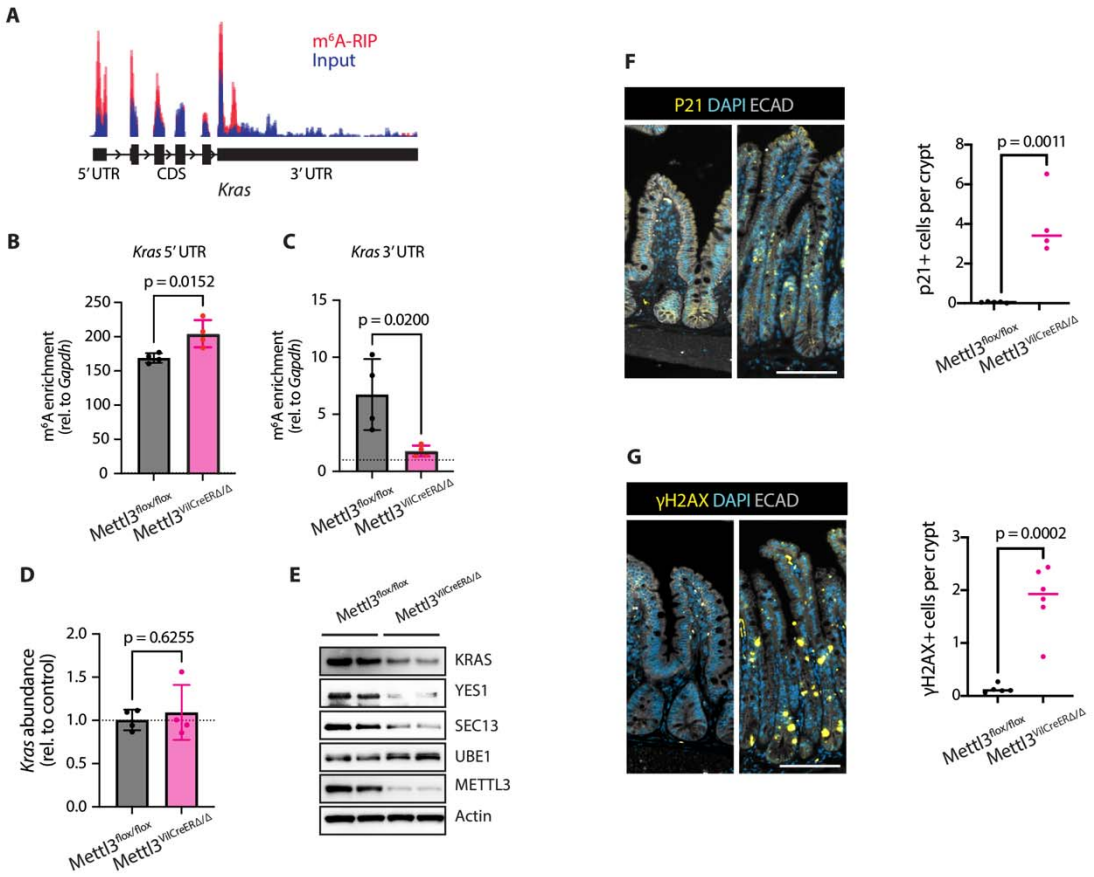

Fig. 7. METTL3 deletion downregulates KRAS and induces cellular senescence. (A) Integrated Genomics Viewer depiction of read density for m^{6}A-RIP (red) and input RNA (blue) for the *Kras* transcript as determined by m^{6}A-seq in distal small intestinal crypts of n=3 wildtype mice. **(B, C)** m^{6}A-enrichment determined by m^{6}A-RIP-qPCR with primers targeting *Kras* 5' and 3' UTR in crypt enriched lysates from *Mettl3$^{flox/flox}$* and *Mettl3$^{VilCreERΔ/Δ}$* mice 3 days post-tamoxifen (n=2M, 2F per genotype). The m^{6}A enrichment score is the result of dividing the ratio of the target-of-interest in RIP compared to RIP input by the ratio of *Gapdh* (negative control) in RIP compared to RIP input. Data presented as median +/- SD. P-value represents unpaired parametric Student's t test. **(D)** qPCR for *Kras* transcript in crypt enriched lysates from *Mettl3$^{flox/flox}$* and *Mettl3$^{VilCreERΔ/Δ}$* mice 3 days post-tamoxifen (n= 2M, 2F per genotype). Data normalized to *Actb* and the mean of *Mettl3$^{flox/flox}$* controls. Data presented as median +/- SD. P-value represents unpaired parametric Student's t test. **(E)** Western blot for top targets with downregulated TE in crypts of *Mettl3$^{flox/flox}$* and *Mettl3$^{VilCreERΔ/Δ}$* mice two days post final tamoxifen injection (n=2 per genotype). **(F, G)** Representative images and quantification of p21 (n=4,4) and γH2AX (n=5, 6) staining in distal half small intestine of *Mettl3$^{flox/flox}$* and *Mettl3$^{VilCreERΔ/Δ}$* mice two days post final tamoxifen injection. Images and quantification from areas of most severe histological distortion in distal small intestine of mice two days post final tamoxifen injection. Each data point is the mean of three representative sections imaged per mouse with bar at median value and p denotes value of unpaired parametric Student's t test. Scale bar 100 µM.

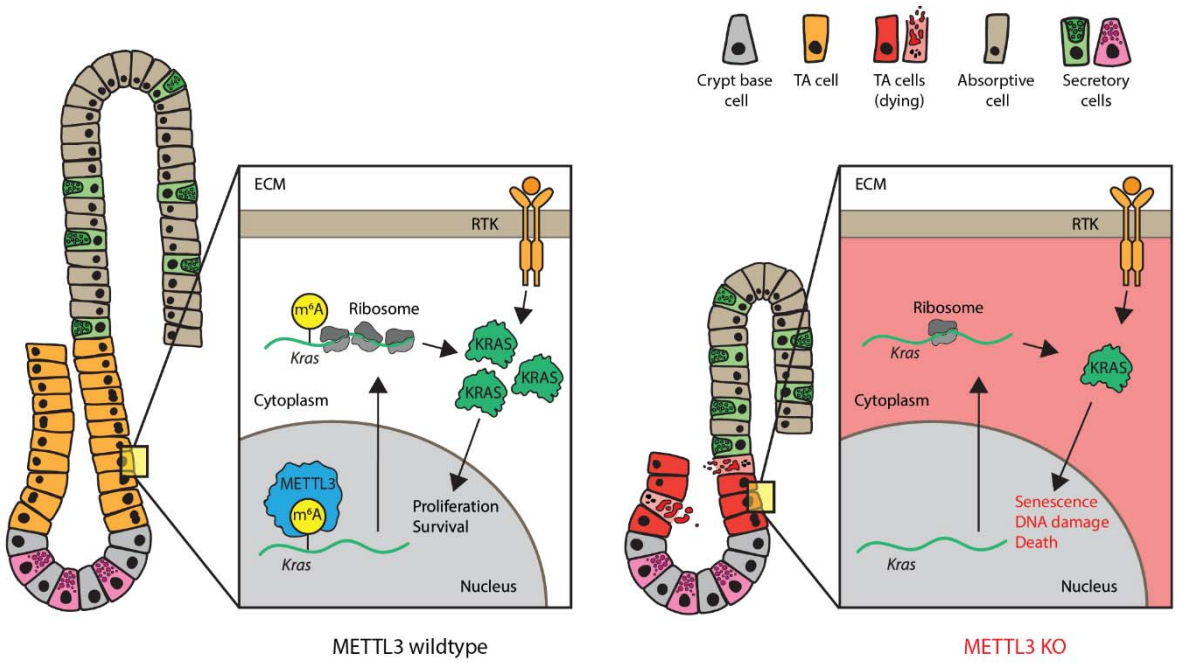

Fig. 8. METTL3 maintains growth factor signaling and survival in proliferating small intestinal epithelial cells. Proposed model. METTL3 methylates *Kras* and other transcripts involved in transducing growth factor signaling. Methylation promotes translation of these transcripts, enhancing proliferation and survival in transit amplifying cells downstream of external growth factors. In the absence of METTL3, a decreased response to extracellular growth factors in METTL3 KO transit amplifying cells leads to cellular senescence and death. Loss of transit amplification results in reduced crypt and villus size and diminished production of absorptive cells. ECM, extra cellular matrix. RTK, receptor tyrosine kinase.

Supplementary Materials for

METTL3 is essential for small intestinal epithelial proliferation via regulation of growth factor signaling including KRAS

Charles H. Danan et al.

*Corresponding author. Email: hamiltonk1@chop.edu

This PDF file includes:

Figs. S1 to S5
Tables S1 to S2

Other Supplementary Materials for this manuscript include the following:
Data S1 to S2

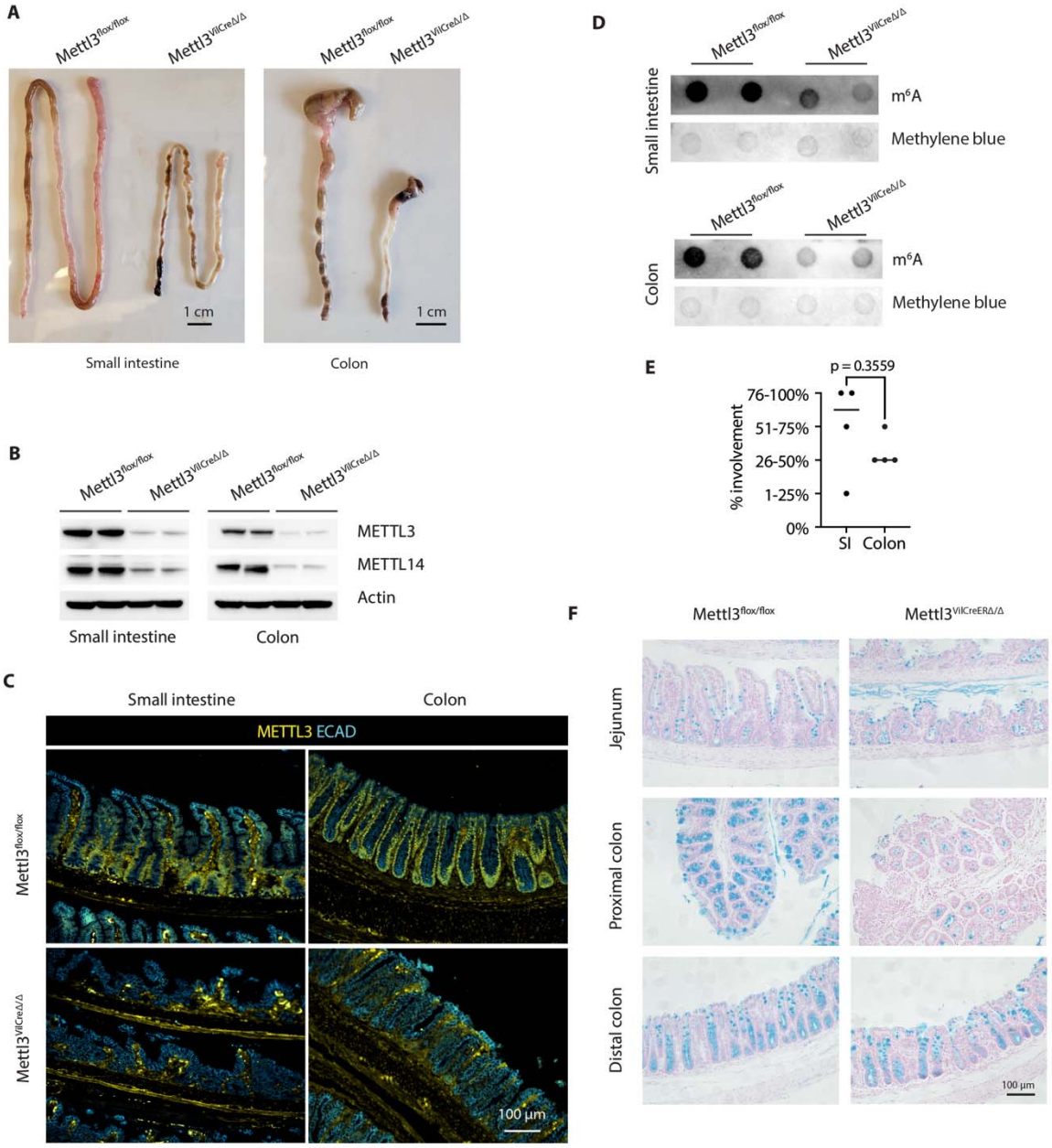

Fig. S1. Verification and additional intestinal phenotypes in *Mettl3*$^{VilCre\Delta/\Delta}$ mice. (A) Representative images of small and large intestine of *Mettl3*$^{flox/flox}$ and *Mettl3*$^{VilCre\Delta/\Delta}$ mice. **(B)** Western blot for METTL3 and METTL14 in epithelial crypt enriched lysates from distal half of small intestine and colon. **(C)** Immunofluorescent staining of METTL3 in jejunum demonstrates epithelial depletion in *Mettl3*$^{VilCre\Delta/\Delta}$ mice. **(D)** m^{6}A dot blot in isolated crypts of distal half of small intestine and colon. **(E)** Greatest percent involvement for any criteria comprising histological score depicted in Fig. 1G or 1I; p denotes value of unpaired parametric Student's t test. Bar at median value. **(F)** Representative Alcian blue staining in small intestine and colon. All data from 29 day old mice.

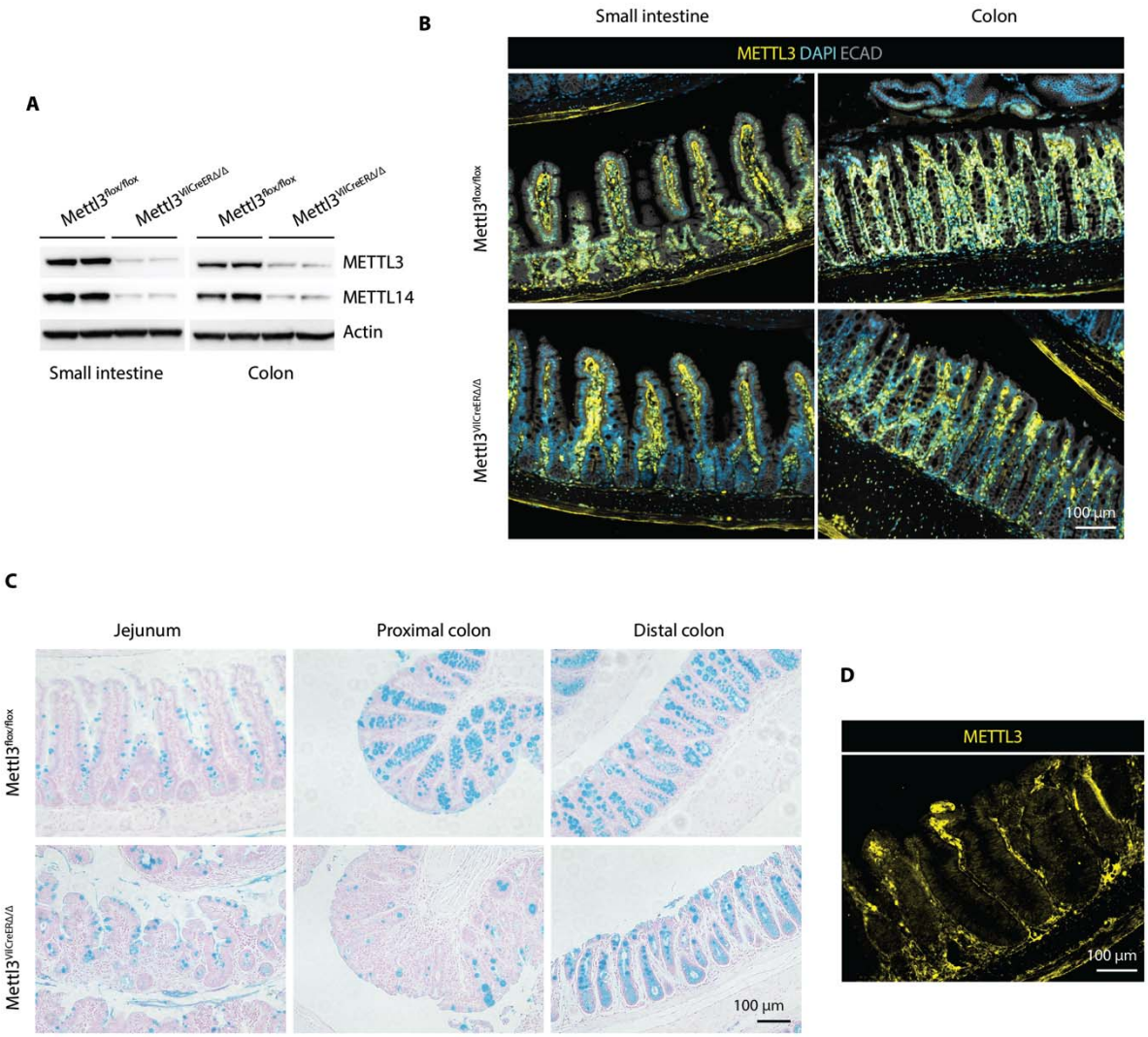

Fig. S2. Validation and additional characterization of inducible *Mettl3*$^{VilCreER\Delta/\Delta}$ mice. (A) Western blot for METTL3 and METTL14 in epithelial crypt enriched lysates from distal half of small intestine and distal half of colon in mice two days post final tamoxifen injection. **(B)** Immunofluorescent staining of METTL3 in jejunum and colon two days post final tamoxifen injection demonstrates epithelial depletion in *Mettl3*$^{VilCreER\Delta/\Delta}$ mice. **(C)** Representative Alcian blue staining nine days post final tamoxifen injection. **(D)** METTL3 staining in hypertrophic small intestinal crypts in a *Mettl3*$^{VilCreER\Delta/\Delta}$ mouse nine days post final tamoxifen injection.

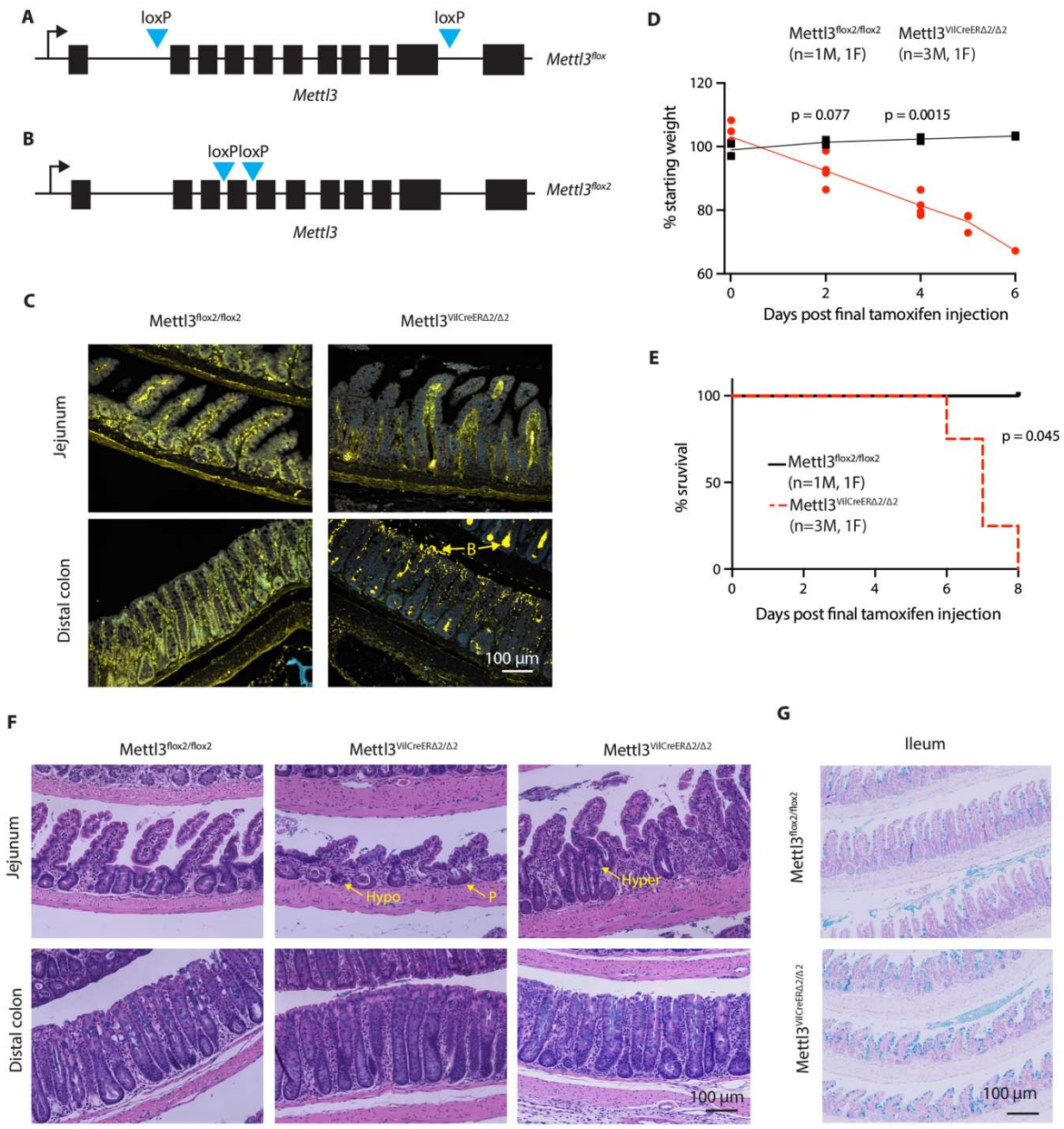

Fig. S3. Alternative deletion of *Mettl3* recapitulates small intestinal and colonic epithelial phenotypes. (A, B) Schematic depicting *loxP* sites within the *Mettl3 gene* in *Mettl3*$^{flox/flox}$ and *Mettl3*$^{flox2/flox2}$ mice. **(C)** Immunofluorescence depicting depletion of METTL3 in jejunum and distal colon. "B" indicates presumed off-target luminal bacterial staining seen with anti-METTL3 antibody. **(D)** Weight loss post final tamoxifen injection in *Mettl3*$^{flox2/flox2}$ (n=2) and *Mettl3*$^{VilCreERΔ2/Δ2}$ (n=4) mice. Each individual point represents one mouse. **(E)** Kaplain-Meier survival curve post final tamoxifen injection in *Mettl3*$^{flox2/flox2}$ (n=2) and *Mettl3*$^{VilCreERΔ2/Δ2}$ (n=4) mice. **(F)** Representative H&E images from small intestine and colon. "Hypo" indicates hypoplastic crypts. "Hyper" indicates hyperplastic crypts. "P" indicates crypts dominated by Paneth cell granules. **(G)** Representative Alcian blue staining of ileum. Images from areas of most severe histological distortion in distal small intestine of mice meeting euthanasia criteria or littermate, tamoxifen-injected controls.

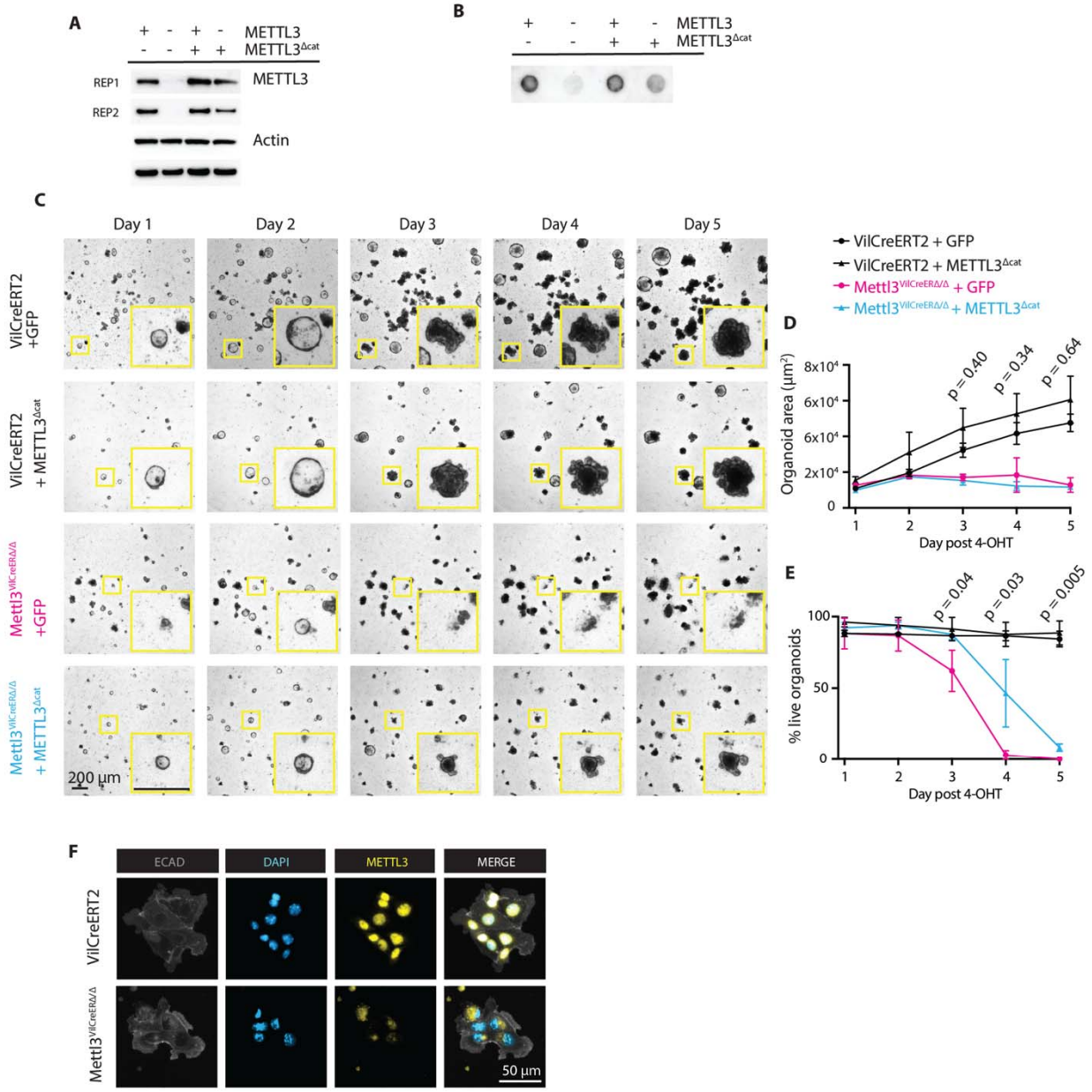

Fig. S4. Catalytic inactive METTL3 does not rescue death of *Mettl3*$^{VilCreER\Delta/\Delta}$ enteroids. (A) Western for METTL3 in *Villin-CreERT2* or *Mettl3*$^{VilCreER\Delta/\Delta}$ expressing GFP (control) or METTL3$^{\Delta cat}$ vector two days post 4-OHT **(B)** m^{6}A dot blot in *Villin-CreERT2* or *Mettl3*$^{VilCreER\Delta/\Delta}$ enteroids expressing GFP (control) or METTL3$^{\Delta cat}$ vector three days post 4-OHT. Each dot is 35 ng isolated mRNA. **(C)** Representative images of enteroid appearance in the five days post 4-OHT treatment in *Vilin-CreERT2* (VilCreERT2) and *Mettl3*$^{VilCreER\Delta/\Delta}$ enteroids expressing either GFP control or METTL3$^{\Delta cat}$ vectors. Individual enteroids highlighted in yellow insets. **(D)** ImageJ quantification of average enteroid 2D area at each day post 4-OHT treatment in enteroids from (C). Each point represents n=3 passage-separated biological replicates. Data presented as mean +/- SD. P-value represents unpaired parametric Student's t test on days 3, 4, 5. P-values shown are for the comparison between *Mettl3*$^{VilCreER\Delta/\Delta}$ + GFP vs *Mettl3*$^{VilCreER\Delta/\Delta}$ + METTL3$^{\Delta cat}$. **(E)** Percent live enteroids at each day post 4-OHT treatment in enteroids from (C). Dead enteroids or colonoids were defined as those being completely opaque, spilling luminal debris, and not demonstrating any growth in the subsequent 24 hours. Each point represents n=3 passage-separated biological replicates. Data presented as mean +/- SD. P-value represents unpaired parametric Student's t test on days 3, 4, 5. P-values shown are for the comparison between *Mettl3*$^{VilCreER\Delta/\Delta}$ + GFP vs *Mettl3*$^{VilCreER\Delta/\Delta}$ +

METTL3$^{\Delta cat}$. **(F)** Whole mount staining of METTL3 in *Villin-CreERT2* and *Mettl3*$^{VilCreER\Delta/\Delta}$ intestinal epithelial monolayers two days post 4-OHT treatment.

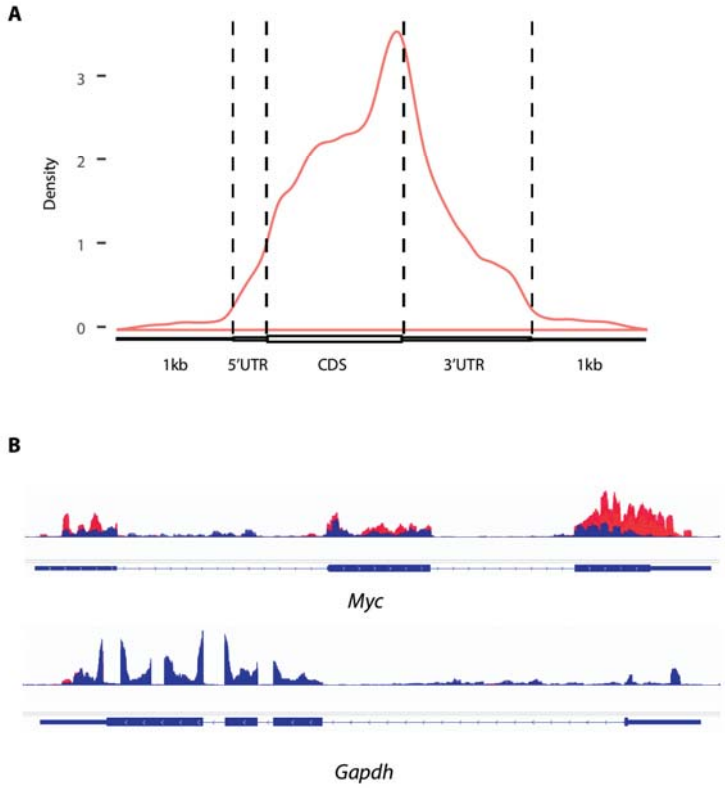

Fig. S5. Quality control for m^{6}A-seq. (A) Metagene density plot depicting distribution of m^{6}A peaks called by Exomepeak2 within m^{6}A-seq data from wildtype mouse small intestinal crypt epithelium. **(B)** m^{6}A-seq read density (red) compared to input RNA read density (blue) for positive control (*Myc)* and negative control (*Gapdh*) transcripts as seen in Integrated Genomics Viewer.

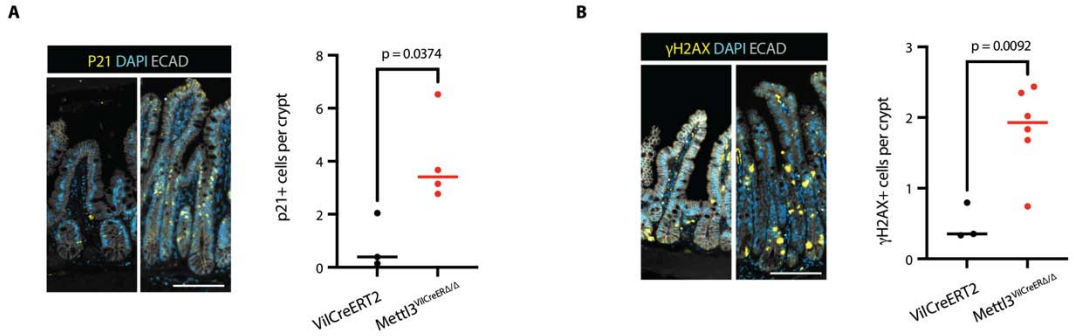

Fig. S6. Increases in cellular senescence and genomic instability after METTL3 deletion are significant compared to *Villin-CreERT2* controls. (A and B) Representative images and quantification of p21 (n=3,4) and γH2AX (n=3, 6) staining in distal half small intestine of *Villin-CreERT2* and *Mettl3*$^{VilCreER\Delta/\Delta}$ mice two days post final tamoxifen injection. Images and quantification from areas of most severe histological distortion in distal small intestine of mice two days post final tamoxifen injection. Each data point is the mean of three representative sections imaged per mouse with bar at median value and p denotes value of unpaired parametric Student's t test. Scale bars 100 µM.

Table S1.

Feature graded	Grade	Description
Inflammation	0	None
	1	Slight
	2	Moderate
	3	Severe
Extent	0	None
	1	Mucosa
	2	Mucosa and submucosa
	3	Transmural
Regeneration	4	No tissue repair
	3	Surface epithelium not intact
	2	Regeneration with crypt depletion
	1	Almost complete regeneration
	0	Complete regeneration or normal tissue
Crypt damage	0	None
	1	Basal 1/3 damaged
	2	Basal 2/3 damaged
	3	Only surface epithelium intact
	4	Entire crypt and epithelium lost
Villus damage (SI only)	0	No change in villus height
	1	25% reduction in villus height
	2	50% reduction in villus height
	3	75% reduction in villus height
	4	Complete loss of villus
Percent involvement	1	1-25%
	2	26-50%
	3	51-75%
	4	76-100%

Table S1. Intestinal mucosal histopathological scoring rubric. Histopathological scoring rubric adapted from (*65*) used for small intestine and colonic histopathological

scoring, with scoring rules added for villus damage (villus damage only assessed in small intestine).

Data S1. (separate file). RNA-seq and Ribo-seq in METTL3 KO enteroids.

Full results of RNA-seq and Ribo-seq from n=3 *Villin-CreERT2* (CTRL) and n=3 *Mettl3*$^{VilCreER\Delta/\Delta}$ (KO) enteroid biological replicates 72 hours after initiating 4-OHT treatment. Green columns and blue columns display transcripts per million (TPM) values output by Kallisto in total RNA and ribosome footprint RNA fractions, respectively. Light orange columns correspond to translational efficiency (TE) values for each transcript determined by dividing the TPM in the total RNA library by the TPM in the ribosome footprint library for each individual transcript and sample. P value refers to the comparison between mean TE of CTRL vs mean TE of KO replicates.

Data S2. (separate file). m6A-seq in wildtype mouse crypt epithelium.

Full output of exomePeak2 analysis of m^{6}A-sequencing data produced in epithelial cells sorted from distal small intestinal crypts of n=3 adult wildtype mice.